Nanoscale

REVIEW

View Article Online
View Journal | View Issue

Cite this: *Nanoscale*, 2018, **10**, 6235

Recent advances in the nanoengineering of electrocatalysts for CO_2 reduction

Fengwang Li, Douglas R. MacFarlane * and Jie Zhang *

Received 26th December 2017,
Accepted 21st February 2018

DOI: 10.1039/c7nr09620h

rsc.li/nanoscale

Emissions of CO_2 from fossil fuel combustion and industrial processes have been regarded as the dominant cause of global warming. Electrochemical CO_2 reduction (ECR), ideally in aqueous media, could potentially solve this problem by the storage of energy from renewable sources in the form of chemical energy in fuels or value-added chemicals in a sustainable manner. However, because of the sluggish reaction kinetics of the ECR, efficient, selective, and durable electrocatalysts are required to increase the rate this reaction. Despite considerable progress in using bulk metallic electrodes for catalyzing the ECR, greater efforts are still needed to tackle this grand challenge. In this Review, we highlight recent progress in using nanoengineering strategies to promote the electrocatalysts for the ECR. Through these approaches, considerable improvements in catalytic performance have been achieved. An outlook of future developments in applying and optimizing these strategies is also proposed.

1. Introduction

Carbon dioxide (CO_2) is an important trace gas in the Earth's atmosphere. As a major greenhouse gas, it plays a vital role in regulating the Earth's surface temperature through the so-called greenhouse effect.[1] In the long term, the carbon cycle, in which carbon is exchanged between the atmosphere, oceans, lands and the biosphere, maintains a balance to keep the Earth's temperature relatively stable, similarly to a thermostat. However, since the start of the Industrial Revolution, the global mean CO_2 concentration has increased by ~45%, from 280 parts per million (ppm) in the mid-18th century[2] to 406 ppm, as measured at the Mauna Loa Observatory (MLO) in Hawaii in February 2017. Another appalling truth is that the rate of CO_2 growth over the last decade is 100–200 times faster than what the Earth experienced during the transition from the last Ice Age.[3] This increase of CO_2 and other greenhouse gases (*e.g.*, methane) in the Earth's atmosphere has been causing a series of problems, including global warming, desertification, and ocean acidification.

This increase of CO_2 is mainly due to anthropogenic activities. Fossil fuels such as coal, petroleum and natural gas are being mined and consumed by human beings at an unprecedented scale and speed to satisfy the energy demand of the rapidly growing world population and economy. The global energy demand reached 18 TW in 2013 and ~81% of this came from fossil resources, according to the International Energy Agency.[4] The demand is projected to further increase to 24 or 26 TW in 2040 with a corresponding rise in CO_2 emissions from 32 Gt per year in 2013 to 37 or 44 Gt per year in 2040.[4] This not only results in huge amounts of anthropogenic CO_2 emissions, but also raises concerns about energy supply due to the non-renewable nature of fossil fuels. Thus, our reliance on fossil fuels must be reduced by developing alternative, renewable energy sources such as solar and wind power.

The past decade has seen a rapid growth of renewable energy, but the percentage of these renewable power sources is still very low in the overall energy consumption. Moreover, most of them are intermittent and geography- or weather-dependent.[5] Unlike traditional power sources with a steady power output, power generation from renewable sources varies significantly over time and often fails to match the energy demand, posing serious threats to the electrical power grid. As a result, additional energy conversion and storage techniques, such as rechargeable lithium batteries, supercapacitors and flow batteries, are required, which, however, are difficult to realize on a grid scale considering their low energy densities and high costs.[6–8] An appealing alternative is the conversion of CO_2 to fuels or value-added chemicals, such as carbon monoxide (CO), formic acid, methanol and methane, using renewable electricity as a power source.[9,10] This strategy holds the potential to address the aforementioned global environment and energy challenges by the storage of energy from renewable sources in the form of chemical bonds in a sustainable manner.[11]

Such an electrochemical CO_2 reduction (ECR) reaction is a multiple proton- and electron-transfer reaction that can take

ARC Centre of Excellence for Electromaterials Science, School of Chemistry, Monash University, Victoria 3800, Australia. E-mail: jie.zhang@monash.edu, douglas.macfarlane@monash.edu

place *via* two-, four-, six- or eight-electron transfer processes.[13] The half-reactions of ECR and the associated standard electrode potentials, E° (V *vs.* the standard hydrogen electrode (SHE)), are summarized in Table 1. As the nature of carbon-containing substrates in aqueous solution varies according to pH, there will be a pH-dependence of equilibrium potential of the respective reactions.

However, the standard potentials shown in Table 1 only indicate the thermodynamic tendency of each reaction and do not indicate the role of kinetics. In fact, ECR does not take place easily, and the actual potentials to drive the reaction are much more negative than the standard electrode potentials (*i.e.*, large overpotentials). The reason for this is that the formation of the intermediate species $CO_2^{\bullet-}$ by transferring one electron to a CO_2 molecule only proceeds as the first step at a highly negative potential, such as −1.97 V *vs.* SHE in dimethyl formamide (DMF) and −1.90 V *vs.* SHE in water.[14–16] The other complicating factor is that the competing proton reduction, or hydrogen evolution reaction (HER), is prevalent in aqueous media, occurring with relatively facile kinetics at 0 V *vs.* SHE, which is comparable to the potentials required for ECRs. Additionally, the thermodynamic reduction potentials for several products of the ECRs are very similar, making it particularly challenging to generate the desired product(s) with high selectivity (*i.e.*, high faradaic efficiency (FE)). Therefore, the development of appropriate catalysts is the primary challenge in the field of the ECR to lower the kinetic energy barriers and steer the selectivity.

Generally, the catalysts for the ECR can be classified into two categories: homogeneous and heterogeneous catalysts. Intensive investigations have focused on the development of molecular complexes with active metal centers and their usage as electrocatalysts homogeneously dispersed in a supporting electrolyte solution. The specific interest in homogeneous catalysts arises from the precise control over the individual catalytic centers afforded by modern synthetic chemistry and therefore the opportunity to study the chemical and structural influences on catalysis. Readers are suggested to refer to several excellent reviews published in recent years for more information.[17–21] In this Review, we will focus on the recent development of heterogeneous catalysts for the ECR.

Table 1 Selected standard electrode potentials for the ECRs (V *vs.* SHE) at 1.0 atm and 25 °C[12]

Half-reactions	Standard electrode potentials (V *vs.* SHE)
$CO_2(g) + 4H^+ + 4e^- = C(s) + 2H_2O(l)$	0.210
$CO_2(g) + 2H^+ + 2e^- = HCOOH(l)$	−0.250
$CO_2(g) + 2H^+ + 2e^- = CO(g) + H_2O(l)$	−0.106
$CO_2(g) + 4H^+ + 4e^- = CH_2O(l) + H_2O(l)$	−0.070
$CO_2(g) + 6H^+ + 6e^- = CH_3OH(l) + H_2O(l)$	0.016
$CO_2(g) + 8H^+ + 8e^- = CH_4(g) + 2H_2O(l)$	0.169
$2CO_2(g) + 2H^+ + 2e^- = H_2C_2O_4(l)$	−0.500
$2CO_2(g) + 12H^+ + 12e^- = CH_2CH_2(g) + 4H_2O(l)$	0.064
$2CO_2(g) + 14H^+ + 14e^- = CH_3CH_3(g) + 4H_2O(l)$	0.084

Although several excellent reviews on this topic have been published,[22–30] most of them are comprehensive summaries of catalysts based on the categories of the materials used or products generated, whereas reports on the optimization strategies to tune the materials for the active and selective generation of a specific product are rare.[31] Recent developments in electrocatalytic applications, such as water splitting, oxygen reduction reaction (ORR), and alcohol oxidation reactions,[32–38] have shown that the catalytic performance of a catalyst is determined by not only the identity of the material but also the optimization strategy applied to tune the material's morphological and electronic structures and surrounding environment on a nanoscale. Therefore, a timely review on the nanoengineering strategies for the optimization of ECR performance is highly desirable, which would also guide the future design of advanced catalysts for the further improvement of their performance for ECR.

This Review starts with a brief summary of the bulk metallic catalysts for the ECR investigated in earlier studies in tandem with the generally recognized mechanism in the ECR. With this background, nanoengineering strategies are then introduced, and different strategies are categorized and reviewed, which is the core purpose of this Review. The motivation for the development of these strategies and the mechanism behind them are highlighted where applicable. We finally conclude with a look at the future challenges and prospects of the nanoengineering exploration of the ECR. It should be noted that this article is not intended to be comprehensive; instead, we would like to highlight some salient developments in recent years, especially with a focus on the last five years.

2. Bulk metallic catalysts for the ECR

Earlier studies of catalysts for the ECR focused primarily on bulk polycrystalline metals. Based on the primary product from ECR, these metals can be divided into four groups: (1) Group 1: Pb, Hg, In, Sn, Cd, Tl, and Bi, which mainly produce formic acid (or formate depending on pH; "formate" is used hereafter to represent both forms).[39–42] (2) Group 2: Au, Ag, Zn, Pd, and Ga, which form CO as the major product.[41,43,44] (3) Group 3: Cu, which is the only metal electrode that is able to produce a wide range of hydrocarbons and oxygenates, such as methane, ethylene, methanol and ethanol, in appreciable amounts, besides CO and formate.[41,45] (4) Group 4: metals, such as Ni, Fe, Pt, and Ti, which catalyze the HER but not the ECR under ambient conditions.[41] However, Jaramillo *et al.*[46] recently demonstrated that the production of methane and methanol is more general than previously thought. They have shown the production of methane on Fe, methane and methanol on Au, Zn, Ni, and Pt, and of methane and methanol (and ethanol) on Ag, albeit in small amounts. The readers are referred to Hori's publications for more details on the bulk metallic catalysts for the ECR.[47,48]

The mechanism for the ECR has been studied experimentally and theoretically over the past few decades to under-

stand the kinetic reaction pathways for different products and the factors governing the selectivity of products over different metals.[19,48–71] Fig. 1 illustrates the possible pathways for the ECR on the different groups of electrodes used. The same as other typical heterogeneous catalytic reactions,[72] the first step is the chemical adsorption of the reactant, CO_2, on the electrode. The formation of CO or formate depends on the initial binding mode of the first intermediate of CO_2 reduction.[58] The mechanistic pathway on Group 1 electrodes, where formate is the major product, has been speculated to proceed *via* a (weakly adsorbed) $CO_2^{\bullet-}$ radical anion that reacts with water to form formate.[73] The catalytic intermediate is expected to bind to the catalyst through (one of) the oxygen atoms and the C atom is therefore available for hydrogenation. In order to achieve a high selectivity towards formate, high overpotentials are needed, as the redox potential for the formation of the $CO_2^{\bullet-}$ is −1.90 V *vs.* SHE.[16] Lowering this overpotential requires the stabilization of the adsorbed $CO_2^{\bullet-}$ intermediate as illustrated in Fig. 1.[58]

Metals in Group 2 and Group 3 bind CO_2 *via* the C atom, that is, the carboxyl intermediate (*COOH, where * denotes an adsorbed species), which is assumed to be formed through a concerted proton–electron transfer to CO_2 (Fig. 1).[55,58,62,66] However, some experimental literature reports indicate that the formation of *COOH takes place *via* the formation of a $CO_2^{\bullet-}$ radical anion (Fig. 1),[41,74] implying the decoupling of proton and electron transfer and therefore a different pH dependence from that of the concerted pathway. On almost all the ECR catalysts, the formation of the $*CO_2^{\bullet-}$ (or *COOH) intermediate through the first electron (and proton) transfer reaction is the rate determining step (RDS).[47] Hence stabilization of this high-energy intermediate is a key to achieving a high-rate and efficient CO_2 reduction process. The carboxyl intermediate will react with the second electron/proton to form the *CO intermediate and water.[70] Both experiments and theory suggest that the binding energy of *CO on metal surfaces determines the overall activity and selectivity of the ECR to produce CO, hydrocarbons or alcohols.[71] For Group 2 metals, the catalysts bind *CO weakly enough for the desorption of CO gas species from the surface, but they should, at the same time, bind *COOH strongly enough to facilitate the activation of CO_2. Too strongly bound CO may poison the catalyst surface, for example, in the case of Pt and Fe in Group 4. Optimum CO binding is required for a catalyst, such as Cu, to proceed to further protonation (formation of *HCO or *COH) to form multi-carbon products *via* a series of complicated proton and electron transfer reactions.[49–51] However, it is a great challenge to optimize the binding energy of each intermediate individually. The binding energies of *COOH, *CO and *CHO are typically correlated through the "scaling relations", *viz.* the binding energy of *CO is positively correlated to that of *COOH and *CHO, making it difficult to control them independently.[49,51,54,71]

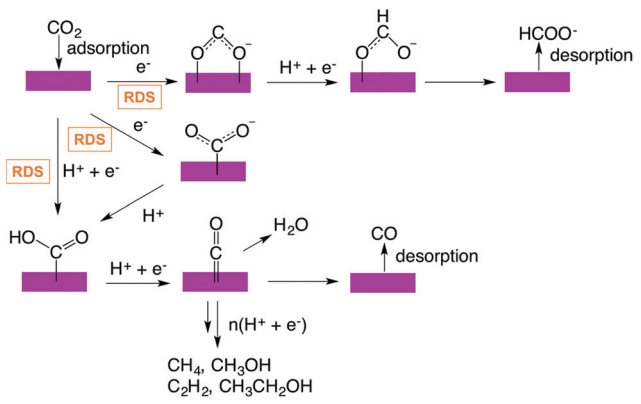

Fig. 1 Possible reaction pathways for the ECR on metals. Redrawn according to ref. 28. The most likely RDS in different pathways is indicated.

3. Nanoengineering of catalysts for the ECR

3.1. Significance of nanoengineering

Significant advances in the development of novel nanocatalysts for electrocatalytic reactions have been made over the past few decades. Nanomaterials often show enhanced catalytic activity compared with that of bulk materials due to their unique morphological, electronic, interfacial and surface chemical properties.[75] These properties can be deliberately tuned to modify the activity and selectivity of electrocatalytic reactions. For example, the size of nanoparticles (NPs) can be used to control the number of coordinatively unsaturated sites on the catalyst surface, which may influence the binding strengths of reactants and intermediates. The shapes of NPs can be used to control the ratio between different crystal facets that may be highly favorable for a particular reaction pathway. In nanoalloy catalysts, more complex mechanisms may come into play. For instance, geometric and electronic effects may alter surface properties by distorting the atomic arrangements or shifting the d-band centers of metal atoms on the catalyst surface.

On the other hand, as heterogeneous electrocatalysis essentially occurs at the interface of an electrocatalyst and a bulk solution, the surface and structure of the catalysts should play a key role in determining the reactant adsorption and electron transfer processes, and in turn, tailor the reaction activity and selectivity. For example, modification of the catalyst surface with small molecules may cause electron donating or accepting effects on the surface electron structure of the metallic NP catalyst, which will tune the adsorption properties of the catalyst and hence the stability of the intermediates in a catalytic reaction. The interaction between the electrocatalyst and the support (*e.g.*, metal oxide and carbon materials) may cause synergistic effects, resulting in interfacial active sites with modulated adsorption properties and stabilization capabilities towards specific reactive species. By thinning a bulk material with layered structures down to a two-dimensional (2D) form, abundant coordinatively unsaturated surface atoms will be exposed at the edges, which may be highly active for specific

catalytic reactions. By optimizing the three-dimensional (3D) electrode geometry, it is possible to expose a greater number of catalytically active sites than in the planar form, promote facile diffusion of species towards and away from these active sites, and shorten electron and ion transport paths as well. "Heterogenizing" homogeneous molecular catalysts by linking them to the surface of a conductive support electrode may provide a combination of the competing advantages of homogeneous catalysts (selectivity and tunability) and heterogeneous catalysts (robustness and easy separation of products from catalysts).

As discussed in greater detail below, these nanoengineering strategies can be classified into three major categories for the optimization of the ECR properties: one strategy aims to modify the intrinsic properties (*e.g.*, lattice and facet) of the electrocatalyst itself, including size and morphology regulation, formation of nanoalloys and use of oxide-derived materials; the second strategy aims to tune the catalyst's performance by introducing surface modification with small molecules or interaction with a support material (*e.g.*, graphene and metal oxide). The third strategy aims to use structural effects to tune the environment surrounding the catalysts, such as pH and CO_2 concentration under catalytic turnover conditions, and to exploit the catalytic capability of molecular catalysts by immobilization on a heterogeneous support.

3.2. Intrinsic property modulation

3.2.1. Nanosize and nanomorphology. Engineering the size of a catalyst to the nanoscale has been regarded as a common and effective way to increase the catalytic capabilities of bulk materials. In a nanosized catalyst, the population of exposed coordinatively unsaturated sites is significantly increased and thus different adsorption properties towards substrates are achieved.[76–78] In contrast to bulk polycrystalline electrodes, the particular interest in nanocatalysts lies in the controllable facets and structures, which allow understanding and accurately correlating their catalytic performance with physicochemical properties. This strategy has been widely used to optimize activities in a range of electrocatalytic reactions, such as CO oxidation, HER, oxygen reduction reaction (ORR) and oxygen evolution reaction (OER).[33,36,79] Recently, nanocatalysts with well-defined size and morphology have shown improved activities for the ECR.

Sun, Peterson and coworkers have synthesized a series of monodispersed Au NPs with different sizes (4, 6, 8 and 10 nm) to investigate the size-dependent catalytic activity and selectivity for the reduction of CO_2 to CO (Fig. 2a).[80] Smaller Au NPs could deliver higher overall mass activity (for the HER and ECR), but lower selectivity towards the ECR (Fig. 2b). 8 nm Au NPs exhibited the highest FE for CO, up to 90% at −0.67 V *vs.* RHE in CO_2-saturated 0.5 M $KHCO_3$. The authors used density functional theory (DFT) calculations to explain such a size-dependent activity and selectivity for the Au NPs. They found that corner sites bind *H more strongly and hence favor the HER, whereas edge sites favor the ECR because of stronger *COOH binding (Fig. 2c). Consequently, 8 nm Au NPs with the lowest corner to edge site ratio show a maximum FE for CO.

Another research study found that the overall current density increased as the Au NP size decreased, but the selectivity for the ECR dropped.[82] According to DFT calculations, the authors attributed these trends to the increase in the number of coordinatively unsaturated sites on small NPs, which favor

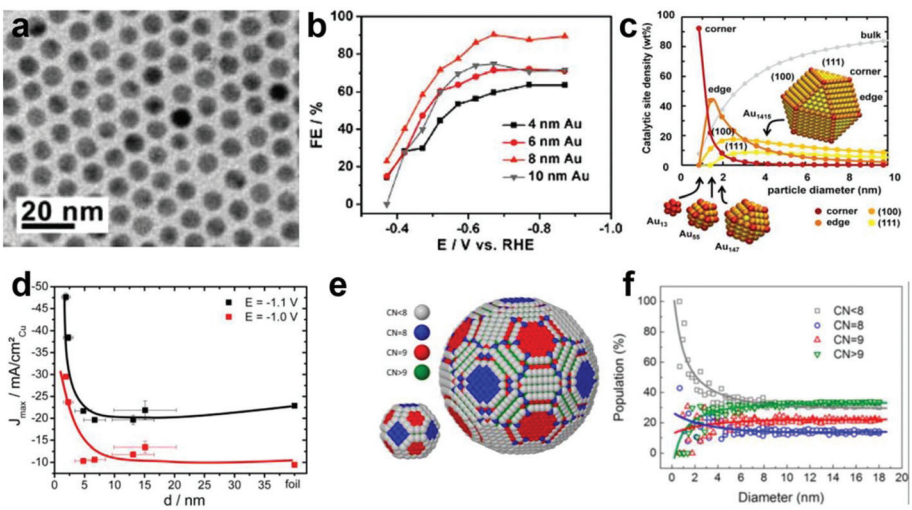

Fig. 2 (a) TEM of the 8 nm Au NPs. (b) FEs for CO of the Au NPs loaded on carbon. (c) Density of adsorption sites (yellow, light orange, dark orange, or red symbols for (111), (001), edge, or corner on-top sites, respectively) on closed-shell cuboctahedral Au clusters *vs.* the cluster diameter. The weight fraction of Au bulk atoms is marked with grey dots. Adapted with permission from ref. 80. Copyright 2013, American Chemical Society. (d) Particle size effect of Cu NPs on the current densities at −1.1 and −1.0 V *vs.* RHE for the ECR. (e) Ball models of spherical Cu NPs with 2.2 and 6.9 nm diameters. Surface atoms are color-coded according to their first neighbor coordination number (CN), CN < 8 (gray), CN = 8 (blue), CN = 9 (red), and CN > 9 (green). (b) Population (relative ratio) of surface atoms with a specific CN as a function of the Cu NP diameter. Adapted with permission from ref. 81. Copyright 2014, American Chemical Society.

the catalysis of the HER over the reduction of CO_2 to CO. Therefore, the CO/H_2 product ratio can be tuned by changing the size of the catalyst particles, which is important for industrial applications, such as the production of syngas.

As discussed in section 2, a moderate binding energy for *CO is vital for the further reduction of *CO to hydrocarbons and alcohols. To probe the size effect on the catalytic performance of Cu towards the ECR, Chorkendorff *et al.*[61] prepared Cu electrodes of different roughnesses (essentially particle sizes) and tested their performance for ECR in 0.1 M $KClO_4$ aqueous solution. It was found that the electrode covered by Cu NPs had better selectivity towards hydrocarbons compared with the electropolished copper electrode or the argon-sputtered Cu electrode. The rougher Cu NP surfaces contained many coordinatively unsaturated sites such as steps, the effects of which can be modelled by the (211) facet in DFT calculations. The (211) surface stabilizes the transformation of *CO into the protonated intermediate *CHO more effectively than either of the (111) and (100) surfaces, dominant forms on the surfaces of the electropolished or argon sputtered Cu electrodes. The authors propose that the activity of Cu could be enhanced further by preparing smaller Cu NPs, as these would have a greater density of coordinatively unsaturated sites.

To study the particle size effects of Cu NPs on the ECR, Cu NPs, 2–15 nm in size, were prepared and used to compare their catalytic activity and selectivity.[81] A dramatic increase in the catalytic activity (Fig. 2d) and selectivity for H_2 and CO was observed with decreasing Cu particle size, in particular, for NPs below 5 nm. Hydrocarbon (CH_4 and CH_2CH_2) selectivity was increasingly suppressed for nanoscale Cu surfaces compared to a bulk Cu electrode. They attributed such activity and selectivity results to the size-dependent surface atomic coordination of Cu NPs. Changes in the population of coordinatively unsaturated surface sites (Fig. 2e and f) and their stronger chemisorption were correlated to the increased H_2 and CO selectivity, higher catalytic activity, and decreased hydrocarbon selectivity. By contrast, Alivisatos *et al.*[83] found that Cu NPs smaller than 30 nm produced hydrogen as the main product while the selectivity towards CO was poor. The conflicting results may come from the different synthesis approaches and measurement conditions employed in these two studies.

Tuning the activity and selectivity towards the ECR was also achieved using NPs of Pd,[84] Bi,[85] Sn[86] and Ag[87] as catalysts. The basic principle is similar, that is, to tune the ratio of edge, corner and terrace sites and therefore to optimize the binding strength of the intermediates *COOH and *CO during the ECR. Such an approach is also supported by DFT calculations.[70]

When the size of the particle decreases to the subnanometer scale (a few atoms and a single atom to extreme conditions), new properties emerge and have been applied to catalysis[88,89] including catalyzing the ECR in very recent years.

Jin's group reported that negatively charged $Au_{25}(SC_2H_4Ph)_{18}^-$ nanoclusters of ~1 nm in diameter with a precisely known crystal structure were able to reduce CO_2 into CO at lower onset potentials, higher current densities, and larger CO production rates than 2 nm, 5 nm, or bulk Au catalysts in CO_2-saturated $KHCO_3$ solution.[90] They attributed the enhancement to the negative charge on $Au_{25}(SC_2H_4Ph)_{18}^-$ because of the ligand, which promotes reactant adsorption, facilitates electron transfer, and boosts electrocatalytic performance. Their follow-up studies supported this hypothesis, where the negatively charged $Au_{25}(SC_2H_4Ph)_{18}^-$ catalyzed the ECR at higher rates and selectivity than that observed for neutral or positively charged ones.[91] Ag nanoclusters also showed better performance for ECR than the bulk Ag electrode.[92]

Recently, a single-atom Ni electrocatalyst, which was synthesized based on ionic exchange between Zn nodes and adsorbed Ni ions within the cavities of a metal–organic framework (MOF), was introduced for the ECR.[93] This single-atom Ni catalyst exhibited a maximum FE for CO production of 71.9% and a current density of 10.48 mA cm^{-2} at an overpotential of 0.89 V in CO_2-saturated 0.5 M $KHCO_3$ solution. By coordinating the Ni atom with nitrogen in carbon-based materials, a $Ni–N_4$ site was constructed by Xie *et al.*,[94] which was able to preserve the active structure to the maximum extent and avoid the agglomeration of Ni atoms into particles. This $Ni–N_4$ structure exhibited high activity for the ECR with a maximum FE for CO of 99% at an overpotential of 0.7 V and a current density of 28.6 mA cm^{-2}. DFT calculations indicated that the introduction of $Ni–N_4$ sites lowers the formation energy of *COOH, which was the RDS in this system, compared with that for N–C. Following a similar strategy, single-atom Ni in a graphene vacancy[95] and atomically dispersed Co atoms anchored on nitrogen-doped porous carbon ($Co–N_2$)[96] have also been found to work as efficient electrocatalysts for reducing CO_2 into CO.

It is reasonable to consider nanowires (NWs) as better catalysts for the ECR as they have more edge sites but fewer corner sites. Indeed, Sun, Peterson and coworkers[97] synthesized ultrathin Au NWs (2 nm wide); a very low onset potential (−0.2 V *vs.* RHE) and a high FE for CO (94% at −0.35 V *vs.* RHE) were achieved on NWs of 500 nm in length (Fig. 3a). DFT calculations indicate that such an outstanding catalytic performance originates from the high ratio of edge sites that maintains activation of CO_2 to *COOH while facilitating the release of *CO (Fig. 3b).

Aside from NWs, nanocatalysts of other shapes have also been developed for the ECR with the purpose of exposing specific crystal facets. Luo *et al.*[98] demonstrated an enhanced current density and a significantly improved FE (96.8%) for CO and energy efficiency (61.7%) over triangular silver nanoplates compared with bulk Ag or similarly sized Ag NPs in 0.1 M $KHCO_3$ solution (Fig. 3c). As suggested by DFT calculations, the shape-dependent electrocatalytic properties originate from the optimum edge-to-corner ratio together with the dominant Ag(100) facet, where lower energy is required to initiate the formation of *COOH, the RDS (Fig. 3d).

Buonsanti *et al.*[99] synthesized two different sized Cu nanospheres (7.5 nm and 27 nm) and three different sized Cu nanocubes (24 nm, 44 nm, and 63 nm) by a colloidal chemistry-based method and exploited the structure–property relation-

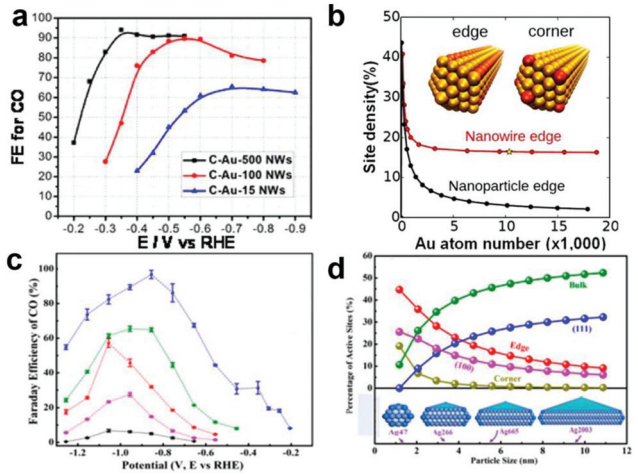

Fig. 3 (a) Potential-dependent FEs for CO of 500, 100 and 15 nm length Au NWs supported on carbon. (b) Edge site weight percentage for a 2 nm wide Au NW and an Au NP as a function of the number of Au atoms. Adapted with permission from ref. 97. Copyright 2014, American Chemical Society. (c) FEs for CO at various applied potentials on glassy carbon (black), carbon black (pink), bulk Ag (red), Ag NPs (green) and triangular Ag nanoplates (blue). (d) Active adsorption site density on triangular Ag nanoplates as a function of particle size. Adapted with permission from ref. 98. Copyright 2017, American Chemical Society.

ship between Cu nanocrystals and their behavior as catalysts for the ECR in 0.1 M $KHCO_3$ solution. Within the same morphology, smaller Cu nanocrystals exhibited higher activity whereas the cube-shaped nanocrystals were more active than the spheres. A non-monotonic size dependence of the selectivity in cube-shaped Cu nanocrystals was revealed in the study. Among the Cu nanocubes of three sizes tested, cubes with 44 nm edge length exhibited the highest selectivity towards the ECR (80%) and FE for ethylene (41%). Statistical analysis of the surface atom density suggests a key role played by edge sites: an optimal ratio of edge sites over (100) plane-sites is crucial to maximize the ECR activity and ethylene selectivity.

Sargent's group also explored the control of the Pd NP morphology to increase their catalytic activity and stability in the electroreduction of CO_2 to formate.[100] Through DFT calculations, they found that higher-index facets with more steps and coordinatively unsaturated atoms in Pd NPs should lead to a greater activity towards the ECR. On this basis, they synthesized branched Pd NPs enclosed by high-index facets, which displayed a record current density of 22 mA cm^{-2} at a low overpotential of −0.2 V with a FE of 97% for formate, much better than the performance of [100] plane-enclosed Pd nanocubes or [110] plane-enclosed rhombic dodecahedra. The findings highlight the importance of morphological control of high-index surfaces for active and selective ECR.

3.2.2. Nanoalloys. As mentioned above, the reaction activity and product selectivity in the ECR are dependent on the binding strength of the key intermediates, such as *HCOOH, *CO and *H (for the competing HER). Changing the composition of a metallic catalyst by alloying with another metal can enhance the performance over that of the solo metal by tuning their stabilization capability towards key intermediates,[53] and therefore has drawn considerable attention over the past few years.

Koper *et al.*[101] designed a Pd-rich Pd–Au alloy with the idea of combining a metal that binds CO strongly (Pd) with a metal that binds CO weakly (Au) to tune the binding energy of the intermediate *CO. They proposed that the reduction of CO_2 into the *CO intermediate is the RDS and higher hydrocarbons were produced by polymerization of $*CH_2$ intermediates adsorbed on the alloy surface. Lewis *et al.*[102] prepared Ni–Ga alloy films of different compositions (NiGa, Ni_3Ga, and Ni_5Ga_3) and found that the alloy films were able to reduce CO_2 into a range of products, including CH_4, CH_3CH_3 and CH_2CH_2, at low overpotentials. This work shows that a unique and tunable reactivity can be obtained for the ECR by the use of bimetals instead of their pure phases, because neither Ni nor Ga alone exhibits low overpotentials for CO_2 reduction. Jaramillo *et al.*[103] synthesized a thin film of Au–Pd alloy and found it more active and selective for $HCOO^-$ production than either pure Au or Pd, which was attributed to a synergistic effect in this alloy. Sun and coworkers developed a Pd–Sn alloy for the selective electroreduction of CO_2 into formate.[104] The catalytic activity and selectivity are highly dependent on the surface electronic structure of the alloy. Formic acid was produced with nearly 100% FE at a low overpotential of 0.26 V on the PdSn alloy with optimal surface Pd, Sn, and O configuration. Meyer *et al.*[105] prepared a Cu–Pd nanoalloy catalyst on an electroactive polymeric film, more than doubling the FE for the reduction of CO_2 to methane compared to that of Cu NPs. They proposed that the enhancement arose from a synergistic reactivity interplay between Pd–H sites and Cu–CO sites during the ECR. A Cu–In alloy prepared by electrochemical deposition of In on rough Cu surfaces was also reported to selectively convert CO_2 into CO with a low overpotential.[106] DFT calculations showed that the In was preferentially located on the edge sites rather than on the corner or flat sites of Cu, and the d-electron nature of Cu remained almost intact. However, the adsorption of H (*i.e.*, the stability of *H) was disfavored on Cu in the presence of In, whereas the stability of *COOH was improved and the CO adsorption energy was not changed substantially. The Takanabe and Wallace groups drew similar conclusions using a Cu–Sn alloy, which is reasonable considering the similar chemical properties of Sn and In.[107,108]

To effectively use the alloying strategy to optimize the ECR performance, the fundamental trends of alloying should be studied. For this, Yang *et al.*[109] used monodisperse Au–Cu bimetallic NPs as a catalyst for the ECR. Pure Cu produced various products as expected, and the incorporation of Au promoted CO evolution, with Au_3Cu showing the best selectivity towards CO generation. The preference for CO formation on Au–Cu alloy NPs was attributed to both electronic and geometric effects. The binding strength of *COOH and *CO is expected to become stronger from Au, Au–Cu, to Cu, as higher d-band levels correlate to stronger binding to transition metals (the electronic effect) (Fig. 4a). Therefore, the activity of CO for-

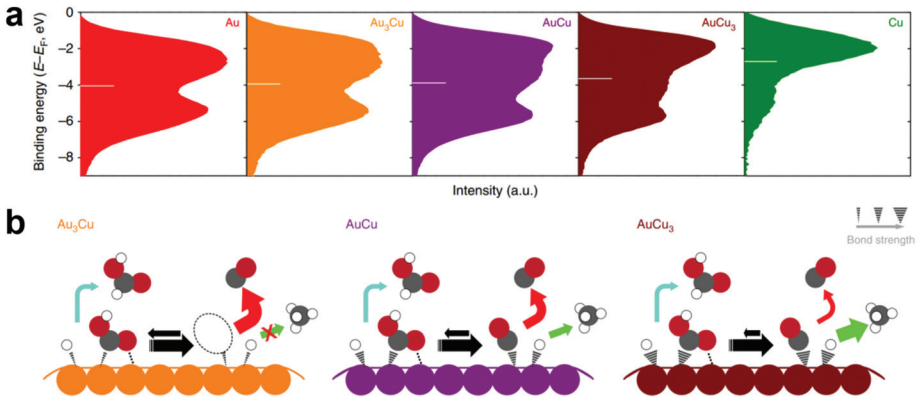

Fig. 4 (a) Surface valence band photoemission spectra of Au–Cu bimetallic NPs. The white bar indicates the center of gravity of the band. The upper limit of integration is fixed at −9.0 eV in binding energy for comparison. (b) Schematic diagram showing the proposed mechanism for the ECR on the surface of Au–Cu bimetallic NPs. Grey colour is C, red colour is O and white colour is H. The relative intermediate binding strength is indicated by the stroke weight (on the top right corner). Additional binding between the *COOH and the catalyst surface is presented as a dotted line. Arrows between the *COOH and *CO are given to show the difference in the probability of having COOH adsorbed on different types of surfaces. Colored arrows indicate the pathway to each product: red for CO, blue for formate and green for hydrocarbons. Larger arrows indicate higher turnover. Adapted with permission from ref. 109. Copyright 2014, Nature Publishing Group.

mation on Au–Cu NPs should lie between those of Au and Cu. However, the results do not follow this trend, indicating that the activity of Au–Cu is not only determined by the electronic effect. The authors proposed that a geometric effect, caused by the local atom arrangement, should also be considered. The intermediate *COOH could be stabilized *via* the Cu–O interaction between the oxygen atom on *COOH and a Cu atom beside the Au atom (Fig. 4b). Hence, Au–Cu NPs are able to stabilize *COOH intermediates better than they stabilizing *CO, which is beneficial for CO formation. Due to the synergistic electronic and geometric effects in Au–Cu alloy NPs, the binding energies of key intermediates can be tuned and optimized, which results in better catalytic performance than that of monometallic catalysts. The same group further studied the effect of atomic ordering degree in Au–Cu alloy on the catalytic performance of the ECR.[110] They showed that ordered Au–Cu alloy NPs could actively and selectively convert CO_2 into CO with a FE of 80%, in contrast to disordered alloy NPs, which were catalytically active for the HER. Using techniques which probed the structure down to the atomic level, the authors ascribed the activity and selectivity to the compressively strained three-atom thick gold overlayers that formed over the intermetallic core, resulting from the disorder-to-order transformation; this hypothesis was further supported by DFT calculations.

Kenis *et al.*[111] also investigated the influence of homogeneity of the alloy on the ECR reactivity. A range of bimetallic CuPd alloy NPs with ordered, disordered, and phase-separated atomic arrangements, as well as two additional disordered arrangements (Cu_3Pd and $CuPd_3$), were studied to determine key factors for the selective generation of C_1 or C_2 products in the ECR (Fig. 5a). They found that, compared with the dis-

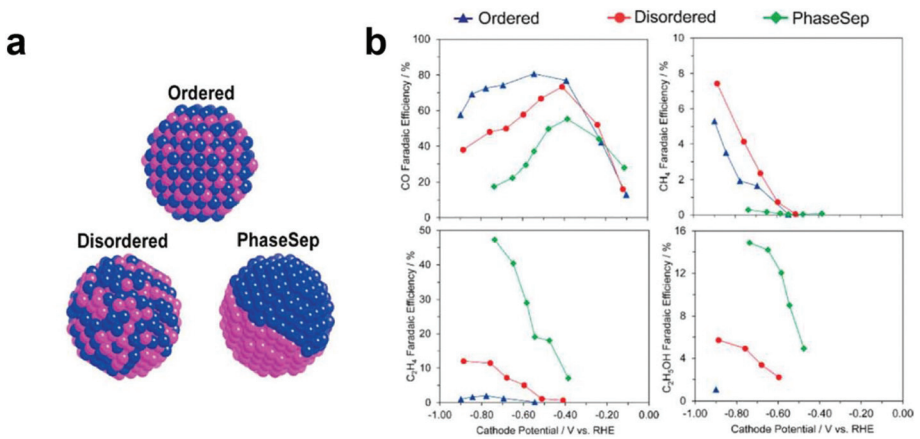

Fig. 5 (a) Illustration of Cu–Pd nanoalloys with different structures. (b) FEs for CO, CH_4, C_2H_4, and C_2H_5OH for Cu–Pd alloy catalysts with different mixing patterns. Adapted with permission from ref. 111. Copyright 2017, American Chemical Society.

ordered and phase-separated CuPd catalysts, the ordered CuPd catalyst exhibited the highest selectivity for C_1 products (>80%), whereas the phase-separated CuPd and Cu_3Pd catalysts achieved higher selectivity (>60%) for C_2 products than seen for either $CuPd_3$ or ordered CuPd (Fig. 5b). Based on these findings, the authors proposed that the probability of dimerization of C_1 intermediates was higher on surfaces with neighboring Cu atoms, implying that geometric effects, rather than electronic effects, were likely to be critical in determining the selectivity of Cu–Pd alloy catalysts.

The interaction between the metal overlayer and the underlying substrate can tune the adsorption energies of the reactant and/or intermediates by the "strain effect" and "ligand effect" (electronic interaction between the overlayer and the substrate), and thus has been used as a powerful strategy in electrocatalysis to optimize the catalytic properties.[112,113] Fermín *et al.*[114] reported the effect of a Pd overlayer on Au NPs on the ECR, while Chorkendorff *et al.*[115] explored the growth of Cu overlayers on a Pt electrode. Koper and coworkers[116,117] also studied Cu overlayers on a Pt electrode and on Au NP cores.

DFT calculations were used to examine how the strain effect and the ligand effect between $Cu_i/M_j/Cu(211)$ and $Cu_i/M(211)$ heterolayers (where M = Rh or Ni, i and j represent the numbers of monolayers) could tune the catalytic properties of the ECR.[118] By comparing the free energy profiles of the CO- and CH_4-formation pathways, the authors found that a Cu monolayer experienced only a pure ligand effect in $Cu_1/M_1/Cu(211)$ and showed a slightly decreased overpotential for the ECR. Other sandwiched surfaces, $Cu_1/Ni_2/Cu(211)$, $Cu_2/Rh_1/Cu(211)$ and $Cu_2/Rh_2/Cu(211)$, in which the ligand effect is weaker, were able to decrease the overpotential further. In the $Cu_1/M(211)$ overlayer, Cu was affected by both the strain and ligand effects, of which the latter dominated. But the strain effect became dominant in the Cu overlayers as the number of Cu monolayers increased from one to three. The tensile strain on Cu in $Cu_{2-3}/Rh(211)$ overlayers was found to result in a significant decrease of overpotential, whereas the compressive strain in $Cu_{2-3}/Ni(211)$ overlayers had the opposite effect. $Cu_2/Rh_2/Cu(211)$ and $Cu_{2-3}/Rh(211)$ increased the catalytic activity while retaining selectivity for CO and CH_4 over the HER.

Yang, Sargent and coworkers[119] recently reported a Cu underpotential deposition (UPD) strategy to quantitatively and systematically tune the coverage of Cu on nanostructured Au electrodes for the ECR. *In situ* surface enhanced Raman spectroscopy (SERS) and DFT calculations indicated that Cu enrichment could directly change the electronic structure of the Au electrode, and therefore alter the molecular coordination environment and binding characteristics of the intermediate *CO on Au surfaces. Such control was used for tuning the relative selectivity of CO formation and the HER to produce syngas. Sun *et al.*[120] demonstrated a Sn-thickness dependent selectivity for the production of either formate or CO using a $Cu@SnO_2$ core–shell NP catalyst. They found that the 1.8 nm SnO_2 shell acted as the SnO_2 NP catalyst for the selective formation of formate, whereas the 0.8 nm SnO_2 shell became selective for CO formation with a maximum FE of 93%. This transformation of selectivity was rationalized by DFT calculations, which suggested that the trace contamination of the SnO_2 surface with Cu caused the uniaxial compression of SnO_2, lowering the formation energy of *COOH and therefore favoring the production of CO over formate. Jiao *et al.*[121] also identified an $Ag@SnO_x$ core–shell NP catalyst that contained an Ag–Sn bimetallic core and an ultrathin partially oxidized SnO_x shell for the ECR. By tuning the thickness of the SnO_x shell, an optimal catalytic activity and selectivity towards formate was achieved at a shell thickness of ~1.7 nm. DFT calculations showed that oxygen vacancies on the SnO(101) surface were crucial for CO_2 activation and the catalytic activity toward formate arose from the competing effects of favorable stabilization of intermediates by lattice expansion and the electron conductivity loss due to the increased thickness of the SnO_x layer.

3.2.3. Oxide derivation. Metallic catalysts derived from the corresponding oxides have recently been identified as promising materials to catalyze the ECR. The treatments are usually carried out through (pulsed) anodization or annealing of the metal electrodes in air, followed by (*in situ*) electroreduction or annealing in the presence of a reductive atmosphere (*e.g.*, hydrogen) to obtain the oxide-derived catalysts.[31] Such obtained catalysts usually possess metastable structures, high-density grain boundaries and high surface areas, which are responsible for the exposure of more catalytically active sites and stabilization of intermediates for the ECR, leading to the improved catalytic activity, selectivity and durability.

Kanan *et al.*[122] prepared Cu electrodes by annealing Cu foil in air and electrochemically reducing the resulting Cu_2O layers (Fig. 6a), and found that the ECR activities of the oxide-derived

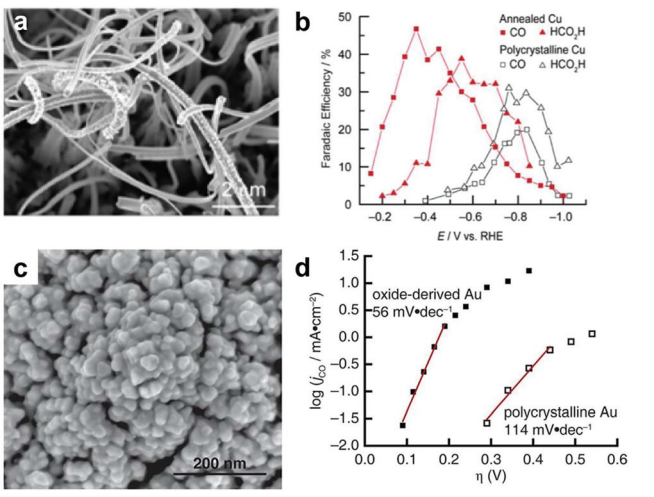

Fig. 6 (a) SEM image of oxide-derived Cu after electrolysis. (b) Comparison of the FEs for CO and formic acid on polycrystalline Cu and Cu annealed at 500 °C for 12 h. Adapted with permission from ref. 122. Copyright 2012, American Chemical Society. (c) SEM image of oxide-derived Au NPs. (d) Tafel plots for polycrystalline Au and oxide-derived Au. Adapted with permission from ref. 123. Copyright 2012, American Chemical Society.

Cu electrodes were strongly dependent on the initial thickness of the Cu_2O layer. Thin Cu_2O layers, formed by annealing at lower temperature, resulted in electrodes with catalytic activity comparable to that of polycrystalline Cu. In contrast, Cu_2O layers formed at higher temperature resulted in electrodes with large roughness factors, which not only required lower overpotentials but also exhibited higher selectivity towards the ECR than that seen for polycrystalline Cu (Fig. 6b). Furthermore, the activity of the oxide-derived electrodes was stable over several hours, whereas a polycrystalline Cu electrode became deactivated within one hour under identical conditions.

The group also used the oxide-derived Cu electrode for the electroreduction of CO to multi-carbon oxygenates (ethanol, acetate and *n*-propanol) with higher selectivity over the HER in CO-saturated alkaline H_2O.[124] By temperature-programmed desorption of CO on the electrode and quantification of the grain boundary density of the oxide-derived Cu NPs, the authors attributed the catalytic activity on oxide-derived Cu to the metastable surface features arising from grain boundaries, which bind CO strongly, distinct from the low-index and stepped facets on polycrystalline Cu.[125,126] Using *in situ* ambient pressure, X-ray photoelectron spectroscopy and quasi *in situ* electron energy loss spectroscopy in a transmission electron microscope, Nilsson's group found that a substantial amount of subsurface residual oxygen but no residual copper oxide existed in nanostructured, oxide-derived Cu electrocatalysts. The subsurface oxygen is supposed to be in a negative oxidation state, which is compensated for by polarization of the conduction electrons in the surrounding metallic Cu atoms. Combined with DFT calculations, the authors proposed that the subsurface oxygen could change the electronic structure of the catalyst and create sites with higher CO binding energy, which was key for reducing CO_2 into multi-carbon compounds.[127]

Baltrusaitis, Mul and coworkers[128] electrodeposited Cu_2O films of different facet orientations and variable thickness on copper plates and used the electrodes for ECR. It was found that reduction of Cu_2O was easier compared to reduction of CO_2 or H_2O, which implies that metallic Cu was the active form in the catalyst. They also found that the selectivity for the ECR on the Cu_2O-derived electrodes was largely dependent on the parent Cu_2O film thickness rather than on the initial crystal orientation. Electrodes from thicker Cu_2O demonstrated a decreased selectivity towards CO_2 reduction but an increased CH_2CH_2 to CH_4 ratio, which was rationalized as a local pH effect. The local pH near the electrode surface during electrolysis is higher than the bulk value due to the consumption of H^+, and the increase in surface roughness, associated with the increased thickness of the Cu films, leads to a higher local pH due to additional surface sites for the HER. Higher local pH favors the formation of CH_2CH_2 from the *CO intermediate over the formation of CH_4. Yeo *et al.*[129] observed a similar trend in the selectivity of CH_2CH_2 and CH_4 and identified an additional C_2 product, ethanol, on their Cu_2O-derived Cu electrodes. In addition to the pH effect, they argued that an optimized surface population of edges and steps on the catalyst was also necessary to facilitate the dimerization of the $*CH_xO$ intermediates into C_2 products. Smith *et al.*[130] prepared Cu NW array electrodes through a two-step synthesis of $Cu(OH)_2$ and CuO NW arrays on Cu foil substrates followed by *in situ* electrochemical reduction to Cu NWs during the ECR. They found that the Cu NW array could reduce CO_2 into CO with a FE of ~50% at an overpotential of 490 mV. The selectivity for CO on a Cu NW array was significantly higher than that on polycrystalline Cu foil under identical conditions, and the improved catalytic properties were ascribed to the enhanced stabilization for the *COOH intermediate.

Kanan's group further investigated the performance of oxide-derived Au, Sn, and Pb electrodes for the ECR.[123,131,132] They found that the oxide-derived Au (Fig. 6c) had a high selectivity for the reduction of CO_2 to CO at very small overpotentials with high durability. Tafel analysis (Fig. 6d) indicated a mechanism that involved a reversible electron transfer to CO_2 to form adsorbed $CO_2^{\bullet-}$ followed by a rate determining proton transfer step, suggesting a better stabilization for the $CO_2^{\bullet-}$ intermediate on oxide-derived Au than on polycrystalline Au. Further studies by the group showed that grain boundaries were responsible for the catalytic property enhancement.[133] They also evaluated the importance of oxide for the ECR on Sn by comparing the activity of Sn electrodes that had been subjected to different pre-electrolysis treatments. It was found that the Sn electrode with a native SnO_x layer exhibited a lower overall current density but significantly higher CO_2 reduction selectivity compared to an electrode with a freshly-exposed Sn^0 surface. On this basis, they prepared a thin film electrode by simultaneous electrodeposition of Sn^0 and SnO_x on a Ti electrode, and found that this electrode demonstrated highly improved activity and selectivity for the ECR compared to that of a Sn electrode with a native SnO_x layer. A Tafel analysis suggested that the presence of SnO_x accounted for the stabilized $CO_2^{\bullet-}$ intermediate. However, they could not determine whether reduction took place at the interface between Sn^0 and SnO_x or on the SnO_x surface directly, and further detailed studies are therefore required.

The oxidation state changes of SnO_2 under catalytic turnover conditions in the process of the ECR are ambiguous, needing further identification. To tackle this, potential- and time-dependent *in operando* Raman spectroscopy was utilized by Broekmann *et al.*[64] They found a strong correlation between the oxidation state of the material surface and the FE of $HCOO^-$ at different alkaline pH levels (Fig. 7a). At moderate cathodic potentials, SnO_2 exhibited a high FE for formate, while at very negative potentials the oxide was reduced into Sn^0 accompanied by a significant decrease in FE for formate. The *in operando* Raman spectroscopy also showed that the kinetic stability region of SnO_2 well exceeded its thermodynamic stability window and the highest selectivity for FE was obtained in a potential range where the SnO_2 was partially reduced into a metastable SnO_x phase (Fig. 7b).

An *in situ* attenuated total reflectance infrared spectroscopy (ATR-IR) study by Bocarsly's group[63] agreed with the presence

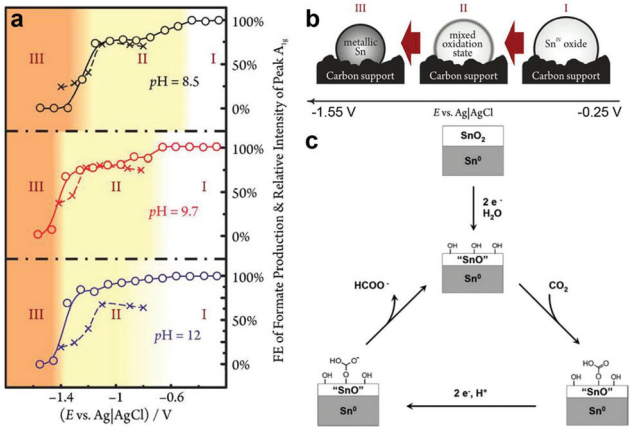

Fig. 7 (a) The relative intensities of the Sn^{IV}-related A_{1g} Raman peaks (○, solid line) and the FEs for formate production (×, dashed line) as a function of the applied potential. In the three distinct potential regions represented by the shaded background, the catalyst is in the form of fully oxidized SnO_2(I), a partially reduced compound of mixed oxidation state(II) and completely reduced metallic Sn(III), as illustrated by the scheme of (b). Adapted with permission from ref. 64. Copyright 2015, American Chemical Society. (c) Proposed mechanism for the reduction of CO_2 to formate on Sn/SnO_x cathodes. SnO denotes a Sn^{II} oxyhydroxide species. Adapted with permission from ref. 63. Copyright 2015, American Chemical Society.

of a metastable oxide layer on the Sn electrode during electrolysis. The potential- and time-dependent IR data indicated the formation and subsequent reduction of a surface-bound carbonate intermediate on the Sn^{II} oxyhydroxide surface formed by partial reduction of SnO_2 (Fig. 7c). This surface-confined tin carbonate was suggested to be the key electroactive intermediate for the production of formate, which is similar to the mechanism found for an In electrode.[134] Ge *et al.*[135] employed DFT calculations to study the impact of SnO_x on tin-based electrode surfaces (modelled by a SnO monolayer on the Sn(112) surface) on the activity and selectivity of the ECR. They also found that, compared to the pure Sn electrode, the formation of SnO_x monolayer on the electrode could promote CO_2 reduction effectively by forming surface hydroxyls. These hydroxyls could react with CO_2 to form a bicarbonate intermediate for the further generation of formate or a carboxyl (*COOH) for the further production of CO.

3.3. Surface modification and support effect

3.3.1. Surface modification. Pioneering studies by Hori and coworkers have demonstrated that different cations and anions in the electrolyte could influence the activity and selectivity of the ECR by affecting the outer Helmholtz plane (OHP) potential of the electrode–electrolyte interface.[136,137] This effect has been recently rationalized in terms of cation hydrolysis occurring in the vicinity of the cathode.[138] With the increase of cation size, the pK_a for cation hydrolysis decreases; the cations serve as buffering agents, lowering the pH near the cathode and leading to an increase in the local concentration of dissolved CO_2. A number of electrolytes and additives, such as ionic liquids, X^- (X = Cl^-, Br^-, I^-), S^{2-} and surfactants, have recently been proposed to influence the ECR through multiple effects, including changes of the local pH, increase of the CO_2 solubility, suppression of the HER, and stabilization of intermediates.[68,139–152] In this section, the focus is on the surface modification of the catalyst rather than on tuning the electrolyte.

Meyer *et al.*[153] used an amine-containing polymer polyethylenimine (PEI) to alter the local environment of N-doped carbon nanotubes (NCNTs) for the selective reduction of CO_2 into formate. It was found that the positively charged polymer could be attached to the surfaces of NCNTs through electrostatic interactions, and a charge transfer from the electron-donating PEI to CNTs was observed, in agreement with previous reports.[154,155] The authors argued that CO_2 was presumably first adsorbed to the basic nitrogen binding sites (pyridinic and pyrrolic N) in NCNTs, where it was reduced into $CO_2^{\bullet-}$. The PEI overlayer worked as a cocatalyst to improve the catalytic capability of NCNTs: the PEI would stabilize $CO_2^{\bullet-}$ by a H-bond interaction, NCNT-N–C(O) $O^{\bullet-}\cdots$H–N-PEI, thus lowering the onset potential for reducing CO_2 into $CO_2^{\bullet-}$. They also proposed that PEI may concentrate CO_2 near the electrode surface from the bulk solution because PEI is known to adsorb CO_2.

Our group found that the addition of PEI could tune the selectivity between H_2 and CO on the amorphous molybdenum sulfide immobilized on reduced graphene oxide (rGO-MoS_x) material.[156] In the absence of MoS_x, the rGO-PEI electrode demonstrated a reduction onset potential about 0.5 V more negative than the rGO-MoS_x electrode in both N_2-saturated and CO_2-saturated $NaHCO_3$ solutions, and only H_2 was detected in the electrolysis in CO_2-saturated $NaHCO_3$ solutions (Fig. 8a), which indicated that MoS_x was an effective catalyst towards the HER in the absence of PEI. It was found that the incorporation of PEI into the rGO-MoS_x system (rGO-PEI-MoS_x), on the other hand, resulted in a high selectivity towards the generation of CO. Hence, a synergetic effect of PEI and MoS_x was responsible for the ECR. Two factors might account for this effect: (1) PEI could suppress the HER and thus enhance the competing ECR, which was evidenced by the inferior HER performance in the presence of PEI in the solu-

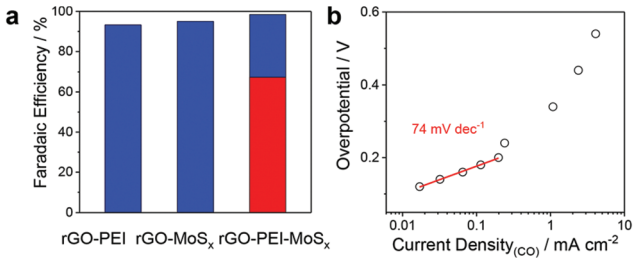

Fig. 8 (a) FEs for CO (red bar) and H_2 (blue bars) of rGO-PEI, rGO-MoS_x, rGO-PEI-MoS_x, potentiostatic electrolysis at −0.65 V in CO_2-saturated 0.5 M aqueous $NaHCO_3$ solution. (b) Tafel plot for the rGO-PEI-MoS_x electrode. Adapted with permission from ref. 156. Copyright 2016, the Royal Society of Chemistry.

tion compared to that without PEI at the same pH. (2) PEI could stabilize the intermediate $CO_2^{\bullet-}$ in the ECR. A much smaller Tafel slope of 74 mV dec^{-1} was obtained with the rGO-PEI-MoS_x electrode (Fig. 8b), which was close to the theoretical value of 59 mV dec^{-1} predicted for the case where a reversible $CO_2/CO_2^{\bullet-}$ process occurs prior to a rate determining chemical step, considering the presence of a competing HER. This enhanced kinetics of the $CO_2/CO_2^{\bullet-}$ process was attributed to the stabilization of $CO_2^{\bullet-}$ by the amines on PEI through hydrogen bonding and electrostatic interactions, in agreement with studies of NCNTs.[153]

Hwang, Min and coworkers[87] synthesized Ag NPs with different sizes on a carbon support using cysteamine as an anchoring agent. They found that the catalyst with 5 nm Ag NPs exhibited a significantly decreased overpotential and the highest ECR activity for the generation of CO (Fig. 9a). DFT calculations suggested limited overpotential modulation by size effects of Ag NPs, in agreement with previous experimental results for the ECR, where the size of Ag or Au NPs changed the current densities significantly but the onset overpotentials remained almost unaffected by the particle size.[80,157] Hence, the authors rationalized the low overpotentials on their catalyst to be the cysteamine anchoring agent, which could induce surface localization of the unpaired electron in the Ag surface *via* the Ag–S interaction (Fig. 9b). Such an altered electronic structure was able to preferentially stabilize the *COOH intermediate with a marginal change in the binding energy of *CO, resulting in an enhanced *COOH stabilization and thus improved catalytic activity. The effect of cysteamine could be understood by the covalency-aided electrochemical reaction (CAER) mechanism,[158] previously proposed by the authors. Furthermore, they compared the effects of amine and thiol functional groups on tuning the selectivity for the ECR with Ag NPs.[159] They found that an amine group on Ag NPs was able to improve CO selectivity by suppressing the HER, whereas the thiol group increased HER activity. This observation was explained by DFT calculations, which showed that attaching amine molecules to Ag NPs destabilized the hydrogen binding and hence suppressed the HER, while an opposite tendency was found with thiol molecules.

Wang *et al.*[161] studied the effects of amino acid (*e.g.*, glycine, leucine, tyrosine, and arginine) modification on the selective electroreduction of CO_2 to hydrocarbons using Cu electrodes. An obvious enhancement in the selectivity of hydrocarbons (C_2H_4, C_2H_6 and C_3H_6) was observed on the amino acid (especially glycine) modified Cu electrodes, regardless of the morphology of the Cu electrodes (NWs, smooth or rough foil). The Tafel slope of the modified Cu electrode was close to 120 mV dec^{-1}, similar to that of the unmodified one, revealing that the modification would not change the RDS of the ECR. The authors suspected that the improved selectivity towards hydrocarbons was related to the strong interaction between the $-NH_2$ groups in amino acids and the key intermediate *CHO in the further reduction steps of *CO into hydrocarbons.[50] DFT calculations were carried out by the authors to confirm this hypothesis; these calculations showed strong hydrogen-bond like interactions of the $-NH_3^+$ end of zwitterionic glycine with both *COOH and *CHO, leading to a stabilization of these two intermediates and therefore enhancement of hydrocarbon generation.

Recently, Chang, Yang and coworkers[160] reported a molecular surface functionalization approach for tuning Au NP catalysts for the ECR (Fig. 9c). They found that the N-heterocyclic (NHC) carbene-functionalized Au NP catalyst could improve both the activity and selectivity for the reduction of CO_2 into CO compared to the parent Au NPs. The author examined the kinetics of CO_2 reduction with Tafel analysis, in which the parent Au NPs gave a slope of 138 mV dec^{-1}, whereas the Tafel slope for carbene-functionalized Au NPs was 72 mV dec^{-1} (Fig. 9d). This indicated that the surface modified electrocata-

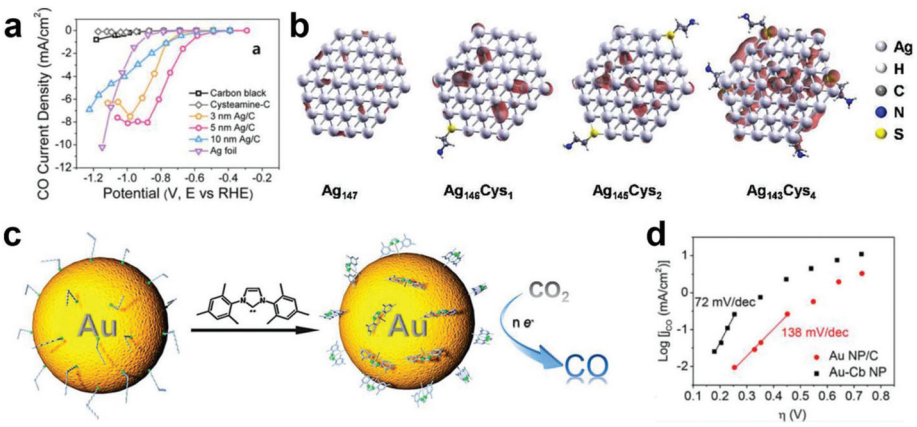

Fig. 9 (a) CO partial current density *vs.* applied potential on different catalysts. (b) Electron spin density. Specific interaction developed in between Ag NP and the cysteamine (Cys_x, *x* denotes the number of cysteamines binding on the Ag NP) leads the unpaired electron to be localized at the surface state of Ag NP. Adapted with permission from ref. 87. Copyright 2015, American Chemical Society. (c) Scheme of surface modification of NHC carbene on Au NPs. (d) Tafel plots for carbene-functionalized Au (Au–Cb) NPs and Au NPs supported on carbon. Adapted with permission from ref. 160. Copyright 2016, American Chemical Society.

lyst underwent a pre-equilibrating one-electron transfer followed by a rate-limiting chemical step. This was in contrast to the unmodified Au NPs, on which a rate-limiting one-electron transfer from the adsorbed CO_2 took place to generate the surface-adsorbed $CO_2^{\bullet-}$. They speculated that carbene coordination would influence the Au surface through a combination of both electronic and geometric effects. Strong σ-donation from the carbenes enriched electrons in the Au NP surface, which would change the mechanism of the ECR. The authors also suggested that the strong carbene–gold bond could destabilize Au–Au bonding with neighboring atoms, leading to restructuring of the Au NP surface and thereby increasing the number of defect sites.

3.3.2. Support effect. The interactions between different components in supported catalysts can result in interfacial active sites with modulated adsorption properties and stabilization capabilities of reactive species caused by the synergy between the support substrate (*e.g.*, metal oxide and carbon materials) and supported NPs.[31,162–164] For example, significantly enhanced catalytic properties at the metal–oxide interface, known as "strong metal–support interaction" (SMSI), have been widely recognized in heterogeneous catalytic processes, such as thermochemical CO oxidation,[165] water–gas shift reaction,[166] thermochemical CO_2 hydrogenation,[167,168] and electrochemical ethanol oxidation.[169] Recently, such a support effect or interfacial interaction has been used to promote the ECR.

Kenis *et al.*[170] studied carbon black- and TiO_2-supported Ag NP catalysts (Ag/C and Ag/TiO_2, respectively) for the reduction of CO_2 into CO. 40 wt% Ag/TiO_2 exhibited a twofold higher current density for CO production than 40 wt% Ag/C in a flow reactor and Ag/TiO_2 exhibited a lower overpotential for the ECR than Ag NPs in cyclic voltammetry tests in a three-electrode cell. On the basis of cyclic voltammetry data, the authors proposed that TiO_2 stabilized the $CO_2^{\bullet-}$ intermediate *via* the participation of the Ti^{IV}/Ti^{III} redox couple while Ag NPs adhered on the TiO_2 surface reduced the intermediate into CO. Bao *et al.*[171] constructed a Au NP–CeO_x interface (Fig. 10a) and showed that the ECR could be significantly enhanced at such an interface, which showed ECR catalytic properties highly enhanced compared to those of Au NPs or CeO_x alone (Fig. 10b). *In situ* scanning tunneling microscopy and photoemission spectroscopy showed that the Au NP–CeO_x interface was the dominant site for enhancing CO_2 adsorption and activation, which could be further promoted by the presence of hydroxyl groups. DFT calculations indicated that the Au NP–CeO_x interface could promote the stability of the intermediate *COOH and thus facilitate the ECR (Fig. 10c). A similar interface-enhanced ECR was further observed on Ag NP–CeO_x, demonstrating the wide applicability of the strategy for the ECR. Using first principles calculations, Xiao *et al.*[62] found that a critical change of the d-band states was obtained when an Ag(111) monolayer was supported on the ZnO(0001) substrate due to the SMSI effect. The binding strength between

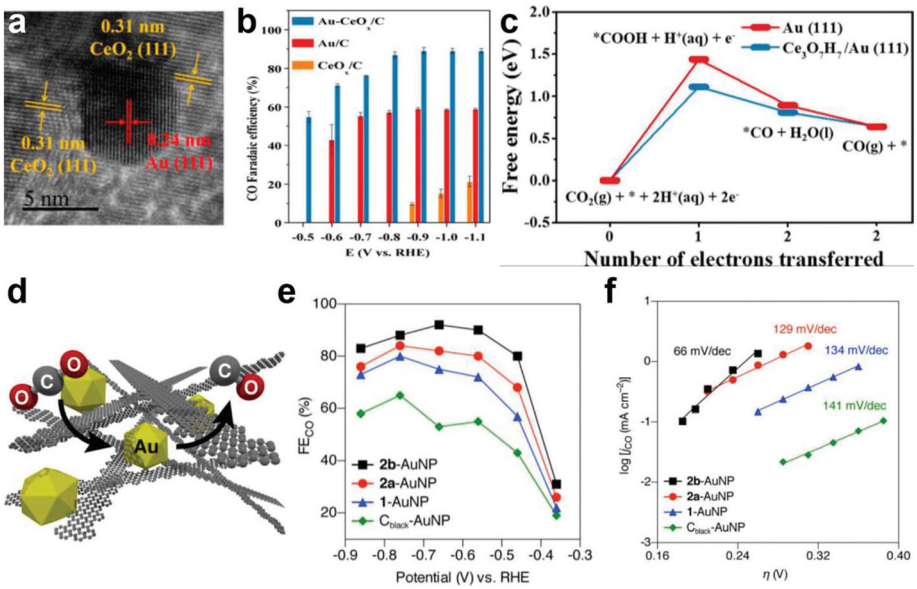

Fig. 10 (a) HRTEM image of the Au–CeO_x catalyst. (b) Potential-dependent FEs for CO over Au/C, CeO_x/C and Au–CeO_x/C catalysts in CO_2-saturated 0.1 M $KHCO_3$ solution. (c) Calculated free energy diagram by DFT of the ECR at 0 V *vs.* RHE on Au(111) and $Ce_3O_7H_7$/Au(111) surfaces. Adapted with permission from ref. 171. Copyright 2017, American Chemical Society. (d) Schematic illustration of the Au NP embedded in GNR catalyst for the ECR. FEs for CO (e) and Tafel slopes (f) of 1-AuNP (chevron GNR-Au NP, blue triangles), 2a-AuNP (cove GNR-Au NP, red circles), 2b-AuNP (Au NP embedded in cove GNR bearing methyl carboxylate groups along its edges, black squares), and C_{black}–AuNP (Au NP supported on carbon black, green diamonds) composite electrodes in CO_2-saturated 0.5 M aqueous $KHCO_3$ solutions. Adapted with permission from ref. 172. Copyright 2017, American Chemical Society.

the supported Ag(111) monolayer and CO_2 was intermediate for the formation of hydrocarbons and/or alcohols.

Fischer *et al.*[172] synthesized a composite material composed of Au NPs embedded in a bottom-up synthesized graphene nanoribbon (GNR) matrix, and observed a performance enhancement for the ECR (Fig. 10d). This composite material had an onset overpotential of ~0.09 V, a maximum FE for CO of >90% (Fig. 10e) and a superior stability of over 24 hours. The electrochemically active surface area suggested that the GNR could facilitate the dispersion of Au NPs while not obstructing access to the catalytically active metal surface. A Mott–Schottky heterojunction at the GNR–Au NP interface was proposed to be formed, where the charges migrated from a lower work function GNR across the interface towards the higher work function Au NPs, increasing electron density at the metal surface and therefore reducing the catalytic onset potential compared to the potential seen for either bare Au NPs or Au NPs supported on other carbon supports. The authors also proposed that the methyl carboxylates along the graphene edges, introduced by the bottom-up synthetic strategy, could stabilize the intermediate during the ECR and therefore shift the rate-determining step from the first electron transfer to the following chemical step (Fig. 10f). Amal *et al.*[173] fabricated a g-C_3N_4-CNTs composite for the reduction of CO_2 into CO with a maximum FE of 60% and a durability of over 50 hours. The enhanced catalytic activity was attributed to the formation of active carbon–nitrogen bonds within the composite, a high specific surface area and improved conductivity. By large-scale screening-based DFT and microkinetics modeling, Sun *et al.*[174] identified that some transition metal dimers (Cu_2, CuMn, and CuNi) could be promising candidates for the ECR when supported on graphene with adjacent single-vacancy sites.

3.4 Structural engineering

3.4.1 3D structure. By constructing a 3D hierarchical electrode geometry, it is possible to expose a greater number of catalytically active sites, promote facile diffusion of species towards and away from these active sites, and shorten electron and ion transport paths as well, resulting in enhanced electrocatalytic performance compared to that seen for planar structures.[175–178] Furthermore, recent developments on the ECR also reveal that the hierarchical 3D structures are able to regulate the local pH and CO_2 concentration, which are critical factors to tune activity and selectivity in the reaction.[179–183]

Amal, Lu and coworkers[184] fabricated a 3D porous Ag foam electrode for direct use as the catalyst for the ECR and showed a high FE for CO of ~95% and a large current density of 10.8 mA cm^{-2} at an overpotential of 0.88 V. The enhanced catalytic performance was attributed to the unique configuration of the 3D porous Ag structure, which offered high conductivity, a large surface area with active sites, and easily accessible pores to allow facile transportation of reactants and products. Tao *et al.*[185] developed a nanoporous Sn foam catalyst, which exhibited high activity and selectivity for the generation of formate. The authors also attributed the improved performance, compared to that of a bulk Sn electrode, to the high surface area and porous structure. A similar strategy was applied to the fabrication of a cyclic-voltammetry-deposited Pd film with porous morphologies and a hierarchical Sn dendrite electrode consisting of a multi-branched conifer-like structure, both of which had enlarged surface areas for enhanced ECR.[186,187] Mul *et al.*[188] designed a porous hollow fiber copper electrode with a compact 3D geometry, which provided a large-area, three-phase boundary for gas–liquid reactions. The performance of this electrode was significantly enhanced compared to that of the state-of-the-art nanocrystalline copper electrodes, and this enhancement was attributed to a defect-rich porous structure as well as favorable mass transport conditions.

Recently, Jiao and coworkers reported a nanoporous Ag (np-Ag) electrode that was able to reduce CO_2 into CO with a FE of 92% at a moderate overpotential of 0.49 V (Fig. 11a–c).[189] The high activity was ascribed to a large electrochemical surface area (approximately 150 times larger) and intrinsically high activity (approximately 20 times higher) compared with polycrystalline Ag. The authors suspected that the intrinsically higher activity was due to the greater stabilization of the $CO_2^{\bullet-}$ intermediate on the highly Ag curved surface, resulting in smaller overpotentials being needed to overcome the thermodynamic barrier. Their follow-up experimental and theoretical works suggested that the kinetic rate-limiting step on this np-Ag electrode was likely to be protonation of the adsorbed *COOH.[190]

Taking advantage of the different transport characteristics of the competing HER and ECR in a weakly buffered medium, it is possible to enhance selectivity towards the ECR by inhibiting the HER. To probe this, Surendranath *et al.*[182] investigated the effect of an Au inverse opal (Au-IO) film of varying thickness on the selectivity of the ECR in CO_2-saturated HCO_3^- media. It was found that the specific activity for the HER diminished by 10-fold with increasing porous film thickness, while the CO evolution activity was largely unchanged (Fig. 11d–f). For electrodes with optimal mesoporosity, 99% selectivity for CO evolution was obtained at overpotentials as low as 0.4 V. The authors ascribed the origin of H_2-evolution suppression in Au-IO films to the generation of diffusional gradients within the pores of the mesostructured electrode rather than to changes in the surface facet or grain size of Au. The group also applied this strategy to Ag inverse opal (Ag-IO) electrodes, showing that a mesostructuring approach could change CO-evolution selectivity from less than 5% to more than 80%.[181]

Smith *et al.*[183] studied the effects of Cu NW morphology on the selectivity of the ECR, and found that local pH modulations caused by the length and density of Cu NWs were the main reason for the selectivity regulation. Cu NW arrays with different lengths and densities were prepared by the *in situ* electrochemical reduction of CuO NW arrays grown on a Cu foil substrate (Fig. 12a). It was found that the selectivity for hydrocarbons (ethylene, *n*-propanol, ethane, and ethanol) on Cu NW array electrodes at a fixed potential could be modulated

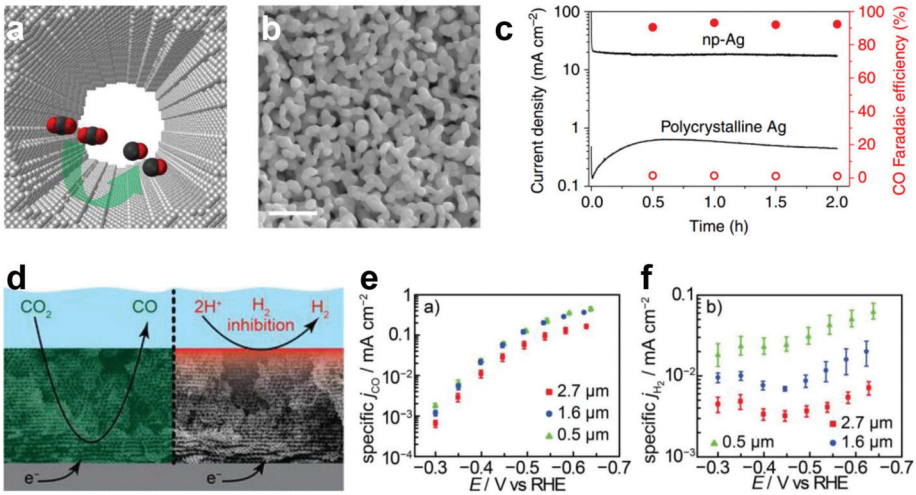

Fig. 11 (a) Schematic diagram of the np-Ag with a highly curved internal surface. (b) SEM of np-Ag, scale bar: 500 nm. (c) Total current density and FE for CO of np-Ag and polycrystalline Ag *vs.* time at −0.6 V *vs.* RHE. Adapted with permission from ref. 189. Copyright 2014, Nature Publishing Group. (d) Schematic diagram of the thickness-dependent ECR and HER activities. Specific activity for CO (e) and H_2 (f) evolution for 0.5 (green triangles), 1.6 (blue circles), and 2.7 (red squares) μm thick Au-IO samples in CO_2-saturated 0.1 M $KHCO_3$ solution. Adapted with permission from ref. 182. Copyright 2015, American Chemical Society.

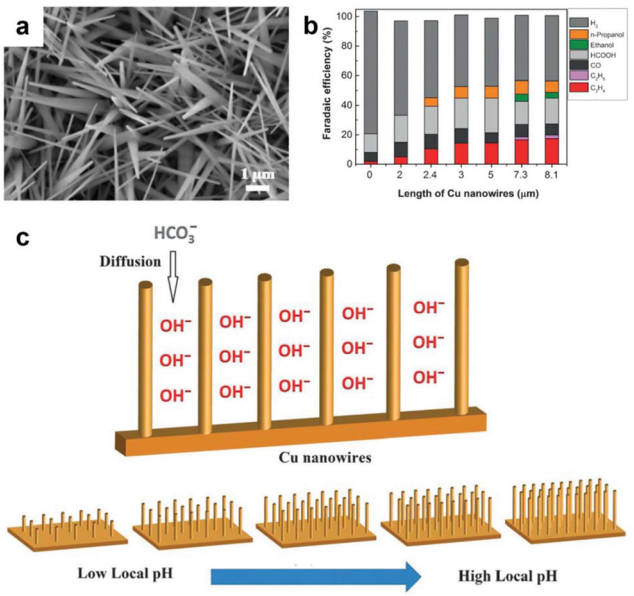

Fig. 12 (a) SEM image of $Cu(OH)_2$ NWs with an average length of 8.1 μm. (b) FEs for C_2H_4, C_2H_6, CO, HCOOH, ethanol, *n*-propanol, and H_2 on Cu NW arrays with different lengths at −1.1 V *vs.* RHE in CO_2-saturated 0.1 M $KHCO_3$ solution (0 mm NW represents Cu foil). (c) Schematic illustration of the diffusion of electrolytes into Cu NW arrays. Adapted with permission from ref. 183. Copyright 2016, Wiley-VCH Verlag GmbH & Co. KGaA.

by varying the NW length and density (Fig. 12b), which resulted in different local pH values. Higher local pH near the surface of longer and denser Cu NW arrays favored the formation of C_2H_4 and alcohols, whereas lower local pH values near the surface of shorter and sparser arrays favored H_2 evolution (Fig. 12c). Wang *et al.*[191] compared two methods to reduce the CuO NWs grown by oxidation of a Cu mesh in air: annealing in the presence of hydrogen or applying a cathodic electrochemical treatment. Their studies showed that these two types of NWs exhibited similar overall current densities but distinctly different selectivities. Compared to polycrystalline Cu and Cu NWs reduced by annealing, the Cu NWs generated by electrochemical reduction demonstrated a significantly increased selectivity towards CO. In addition to the pH effect, the authors attributed the enhanced performance to the presence of a larger proportion of the (100) and (110) facets on the surface of electrochemically reduced Cu NWs than that on the annealed Cu NWs.

To study the effects of Cu electrode morphologies on the selective production of C_2 products (ethylene or ethane) in the ECR, Nam *et al.*[192] prepared Cu mesoporous electrodes with precisely controlled pore widths and depths by a thermal evaporation process on anodized aluminum oxide. Using numerical simulations of electrohydrodynamics, the authors found that nanomorphology could change the local pH and flow velocity by confining the chemicals inside the pores, resulting in prolonged retention time of key intermediates and accelerated C–C coupling reactions. The magnitudes of the flow velocity inside the pores were reduced as the pore width decreased or the pore depth increased, which implied that the CO_2 conversion inside the narrower and deeper pores would proceed more readily. Furthermore, because the ionic concentration inside the narrower pore was hardly affected by vortices, the ionic species inside narrow pores (30 nm) were more abundant than those inside the wide pores (300 nm). Hence, the reagents and reaction intermediates would be trapped more often and for longer durations inside the narrower pores, leading to the prolonged retention time, and this increased the rate of C–C coupling reaction.

Recently, Sargent's group reported that nanostructured electrodes could produce high local electric fields that concentrated electrolyte cations, which in turn led to a high local concentration of CO_2 close to the electrode surface.[179,180] They prepared Au electrodes with the tip radii ranging from large-diameter particles (radius of curvature of about 140 nm) to intermediate-diameter rods (radius of curvature of about 60 nm) to high-curvature nanoneedles (radius of curvature of about 5 nm, Fig. 13a), and evaluated their performance for the electroreduction of CO_2 to CO. The results showed that the partial current density of CO normalized by the electrochemical surface area measured at an overpotential of 0.24 V in a CO_2-saturated 0.5 M $KHCO_3$ solution on Au needles was 63 times higher than that on rods and 112 times higher than that on particles, indicating higher intrinsic ECR activities for Au needles (Fig. 13b). The authors associated this significantly enhanced performance on Au needles with the high local electric fields. DFT calculations showed that adsorbed K^+ ions could lower the thermodynamic energy barrier for the reduction of adsorbed CO_2 into the intermediate *COOH for all Au crystal facets, and a greater electron density was found on the carbon of *COOH in the presence of adsorbed K^+ (Fig. 13c), suggesting a stronger C–Au bond that could modulate the ECR process. Quantitatively mapping the surface adsorbed K^+ ion density in the Helmholtz layer of the electrical double layer directly adjacent to the electrode surface indicated a 20-fold increased surface-adsorbed K^+ ion concentration at the Au needle tip due to the locally-enhanced electrostatic field (Fig. 13d). In contrast, a six-fold increase in the bulk K^+ concentration in the electrolyte only doubled the field-induced K^+ ion concentration near the electrode. With concentrated K^+, CO_2 could be quickly stabilized on the sharp Au tips, where the ECR mostly occurred. This field-induced reagent concentration (FIRC) strategy could also be applied to other catalysts, such as Pd. Besides the FIRC effect, the group also found that the morphology of nanostructured electrodes enhanced long-range CO_2 transport *via* their influence on gas-evolution.[193] Sharper needle morphologies could nucleate and release bubbles as small as 20 μm, leading to a four-fold increase in the limiting current density compared to that found on a NP-based catalyst.

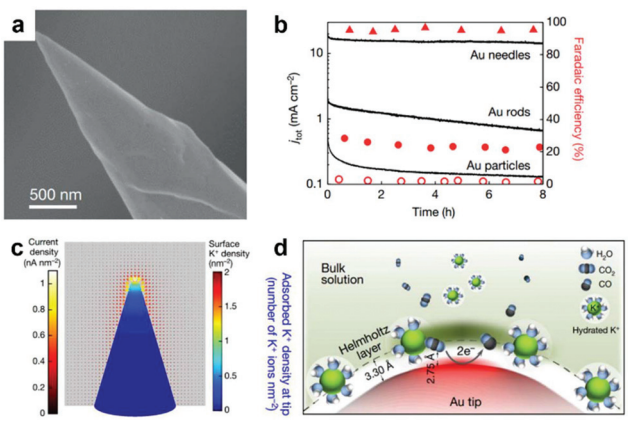

Fig. 13 (a) SEM image of an Au nanoneedle. (b) Total current density and FEs for CO of Au needles, rods and particles *vs.* time at −0.35 V *vs.* RHE. (c) Surface K^+ density and current density distributions on the surface of Au needles. The tip radius is 5 nm. (d) A schematic diagram showing how K^+ ions on the gold surface help CO_2 molecule adsorption. Adapted with permission from ref. 180. Copyright 2016, Nature Publishing Group.

3.4.2. 2D engineering. As new synthesis methods are developed, and following the tremendous interest in graphene, 2D materials including transition metal dichalcogenides (TMDCs, *e.g.*, MoS_2 and WSe_2), transition metal oxides (*e.g.*, MnO_2 and MoO_3), graphitic carbon nitride (g-C_3N_4), hexagonal boron nitride (h-BN), transition metal carbides, carbonitrides and nitrides (MXenes), elemental nanosheets (*e.g.*, phosphorene and silicene) and MOF nanosheets have emerged as appealing functional materials for various applications in electronics, energy and catalysis, due to their unique physical and chemical properties compared to those of their parent bulk counterparts.[194–216]

TMDCs, especially MoS_2, have been widely employed as catalysts for the HER over the past decade.[217–219] The activity of MoS_2, especially after nanoengineering of the bulk material, arises from the active edge sites.[220,221] Recently, DFT calculations by Nørskov *et al.* suggested that the edge sites of MoS_2 and $MoSe_2$ were also active for the ECR due to the different scaling relationship of adsorption energies between key reaction intermediates (*COOH, *CO, and *CHO) on the edges compared to those seen in bulk transition metals.[222] The calculations indicated that the bridging S and Se atoms could selectively bind the intermediates *COOH and *CHO over *CO, resulting in deviation from the scaling relationship among the intermediates and therefore promoting the formation of CO. Moreover, due to the fact that S edges in MoS_2 are easily doped with transition metals, one can finely tune the binding energies of the intermediates by doping.[223] The authors studied the activity of the Ni-doped S edge of MoS_2 for the ECR, and found that the doped S edge had a moderately higher *CO binding energy than the undoped one, accelerating the further reduction of CO into hydrocarbons and/or alcohols. Further theoretical studies by the same group showed that the deviation from the scaling relationship of Ni-doped MoS_2 arose from the doping metal and sulfur binding sites, which have two different linear scaling relationships.[224] When the strongest binding site for each adsorbate is considered, *CO binds on the doping metal site while *COOH, *CHO and *COH bind on the covalent site, sulfur, and the CO* binding energy is significantly weaker than those of COOH* or CHO*. This trend results in an overall deviation from the linear scaling seen on pure transition-metal surfaces, and thus promotes the further reduction of *CO into hydrocarbons and/or alcohols.

Experimentally, Salehi-Khojin *et al.*[225] studied the ECR on MoS_2 in a water–ionic liquid (1-ethyl-3-methylimidazolium tetrafluoroborate, BMIM-BF_4) mixture solution, and found that the layer-stacked bulk MoS_2 with Mo-terminated edges had an excellent performance for the reduction of CO_2 to CO with superior activity, selectivity and durability compared to that of

either bulk Ag or Ag NPs under identical conditions (Fig. 14a). Furthermore, DFT calculations indicated that such a catalytic performance arose from the Mo-terminated edges of MoS_2, which had a high metallic-like d-electron density, taking part in the reactions. Based on this understanding, the authors then synthesized vertically aligned MoS_2 nanosheets with more catalytically active Mo atoms on the edges (Fig. 14b). As expected, a further improvement in the CO_2 reduction current density was observed on this catalyst (Fig. 14c).

Following this work, the same group further prepared a series of nanostructured TMDCs, including MoS_2, WS_2, $MoSe_2$, and WSe_2 nanoflakes (NFs), and evaluated their catalytic properties toward the ECR in a water–ionic liquid mixture (1 : 1 by volume) solution.[226] Among these NFs, WSe_2 exhibited the best ECR performance for the formation of CO (Fig. 14d–f), which was explained by both experimental and theoretical approaches. The lowest work function suggested the superior electronic properties of W edge atoms in WSe_2, resulting in faster electron transfer and consequently higher catalytic activity during the ECR. Using DFT calculations, the authors found that the formation of the intermediate *COOH was exergonic because of strong binding to the TMDC metal edge sites and that the d-band centers of these metal edges were much closer to the Fermi level than those of the Ag(111) surface, also supporting the strong binding of the adsorbed intermediates to the metal edges in TMDCs. They also pointed out the important role of the ionic liquid, which could help transport CO_2 to the catalyst surface by complexation under acidic conditions and increase the local CO_2 concentration.

Given that the d-band electronic structure plays an important role in the enhancement of the ECR, as evidenced above, Xie's group synthesized a MoSeS alloy monolayer catalyst with shortened Mo–S and lengthened Mo–Se bonds to tailor the electronic structure of the Mo atoms.[227] DFT calculations illustrated an increased density of states near the conduction band edge of MoSeS; this resulted in a faster electron transfer, as confirmed experimentally by a lower work function and a smaller charge-transfer resistance. The calculations also showed the off-center charge around Mo atoms, which not only stabilized the COOH* intermediate but also facilitated the rate-limiting *CO desorption step. As a result, MoSeS alloy monolayers delivered a higher selectivity towards CO than either MoS_2 or $MoSe_2$ monolayers.

Recently, Xie's group identified that, by engineering Co_3O_4 to few-layer Co_3O_4 nanosheets[230] or partially oxidized 2D Co nanosheets (Fig. 15a–e),[228] the ECR-inactive cobalt-based material could be transformed into an electrocatalyst with superior activity and selectivity for the reduction of CO_2 into formate (Fig. 15f). The onset overpotential was only 0.07 V, comparable to that achieved with precious Pd NPs on a carbon support. The partially oxidized 2D Co nanosheets could achieve a very high FE of 90.1% for formate generation at an overpotential of only 0.24 V with negligible current density and FE losses over 40 hours. The authors suggested that the increase in surface area and the change in oxidation state synergistically contributed to the adsorption of CO_2 to the surface of the catalyst, which was evidenced by a Tafel slope close to 59 mV dec^{-1}. Their further studies showed that the oxygen vacancies played an important role in tuning the

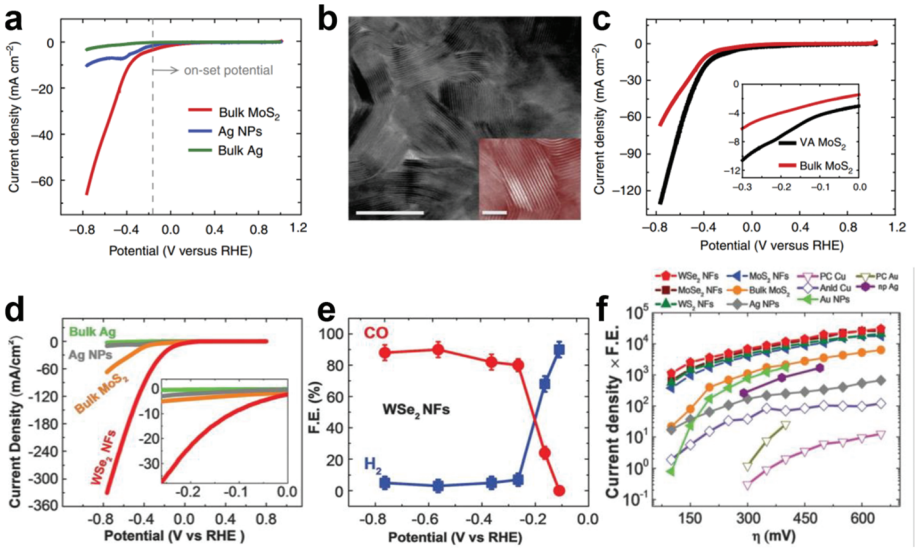

Fig. 14 (a) CV curves for bulk MoS_2, Ag NPs and bulk Ag in CO_2-saturated 96 mol% water and 4 mol% BMIM-BF_4 solution. (b) STEM images of vertically aligned MoS_2 (VA MoS_2), scale bar: 20 nm. The inset is an enlarged image, scale bar: 5 nm. (c) CO_2 reduction performance of bulk MoS_2 and VA MoS_2. Reproduced with permission from ref. 225. Copyright 2014, Nature Publishing Group. (d) CV curves for WSe_2 NFs, bulk MoS_2, Ag NPs and bulk Ag in CO_2-saturated water + BMIM-BF_4 (1 : 1 by volume) solution. The inset shows the current densities at low overpotentials. (e) FEs of CO and H_2 at different applied potentials for WSe_2 NFs. (f) Overview of different catalyst performances at different overpotentials. Reproduced with permission from ref. 226. Copyright 2016, the American Association for the Advancement of Science.

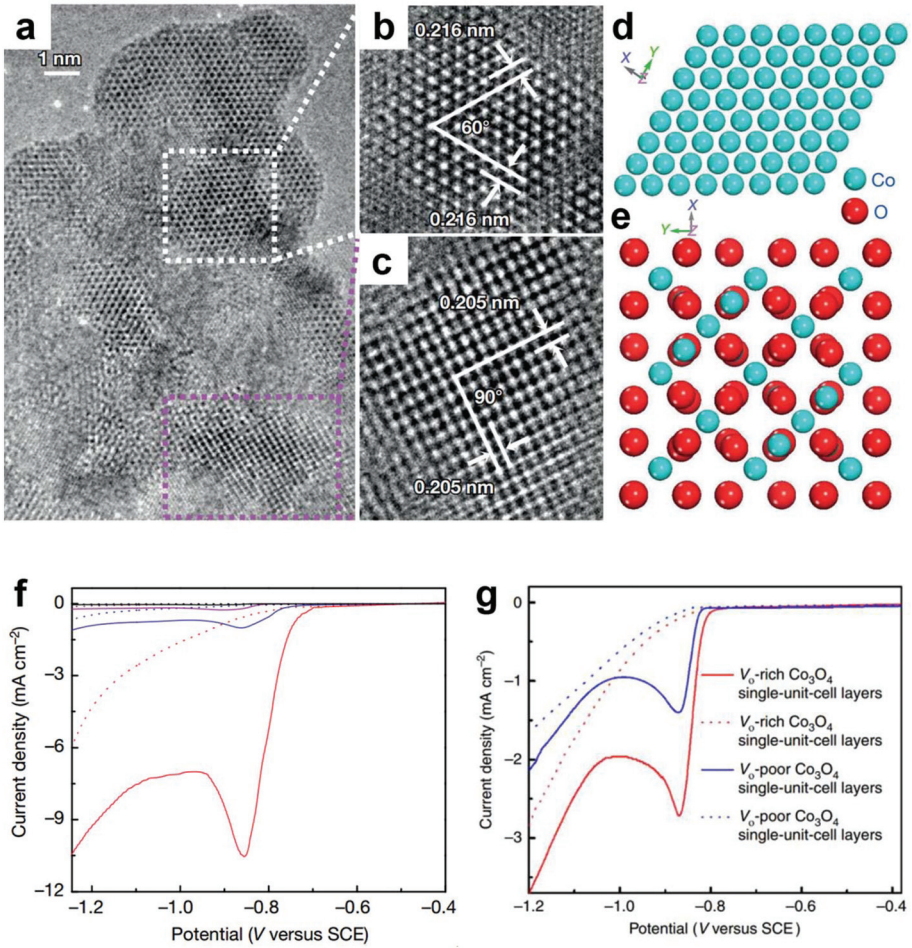

Fig. 15 (a) High-resolution TEM image of partially oxidized 2D Co nanosheets. (b, c) Enlarged TEM images from (a). (d, e) The related schematic atomic models, showing the distinct atomic configurations corresponding to hexagonal Co and cubic Co_3O_4. (f) Linear sweep voltammetric curves of partially oxidized 2D Co nanosheets in CO_2-saturated (solid line) and N_2-saturated (dashed line) 0.1 M Na_2SO_4 aqueous solutions. Reproduced with permission from ref. 228. Copyright 2016, Nature Publishing Group. (g) Linear sweep voltammetric curves of oxygen vacancy rich (V_o-rich) and poor (V_o-poor) Co_3O_4 single-unit-cell layers in a CO_2-saturated (solid line) and an N_2-saturated (dashed line) 0.1 M $KHCO_3$ aqueous solution. Reproduced with permission from ref. 229. Copyright 2017, Nature Publishing Group.

activity and selectivity for the ECR on these 2D cobalt oxide based materials (Fig. 15g).[229] DFT calculations demonstrated that the presence of oxygen vacancies lowered the rate-limiting activation barrier *via* stabilizing the $CO_2^{\bullet-}$ intermediate, confirmed by the lowered onset potential and decreased Tafel slope.

Our group has recently reported the production of 2D "few-layer" antimony nanosheets (SbNSs) by a cathodic exfoliation method (Fig. 16a).[231] The application of such exfoliation turns Sb, an inactive material for CO_2 reduction in its bulk form, into an active 2D electrocatalyst for the reduction of CO_2 into formate with high efficiency. The FE for formate reached a maximum of about 84% at −1.06 V (overpotential of 0.97 V for formate, Fig. 16b) in 0.5 M $NaHCO_3$ solution. The high activity was attributed to the exposure of a large number of catalytically active edge sites. Moreover, this cathodic exfoliation process can be coupled with the anodic exfoliation of graphite in a single-compartment cell for *in situ* production of a few-layer Sb nanosheet and graphene composite (SbNS-G). This composite demonstrated a further improvement in the ECR performance, as evidenced by the highest partial current density for formate (Fig. 16c). The observed increased activity of this composite was attributed to the strong electronic interaction between graphene and Sb. A redshift of both E_g and A_{1g} peaks was observed in the SbNS-G sample (Fig. 16d) due to the n-type doping from graphene to the SbNS. The strong electronic interaction of SbNS with graphene could tune the adsorption energies of the reactant and/or intermediates on the SbNS, hence modulating the reaction kinetics of the ECR.

By introducing heteroatoms (*e.g.*, N, P, S, P, B, and F), graphene-based materials have shown considerable catalytic activities as metal-free electrocatalysts for various energy-conversion reactions, such as the HER, ORR and OER.[195,211,232–242] Very recently, heteroatom-doped graphene has been investigated to catalyze the ECR. Ajayan *et al.*[239] reported a graphene foam incorporated with nitrogen defects as a metal-free elec-

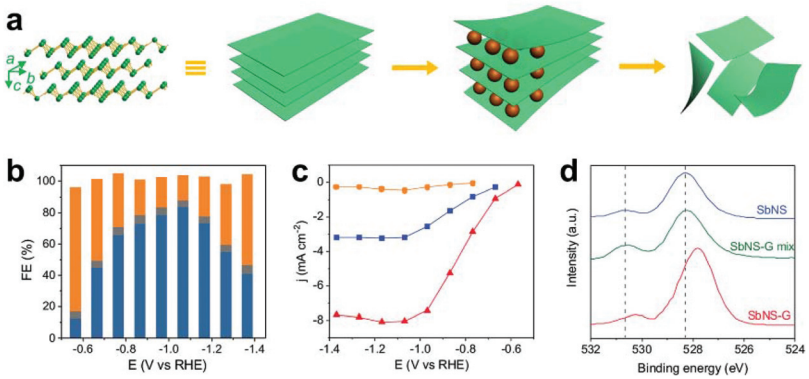

Fig. 16 (a) Side view of the Sb crystal structures and schematic illustration of the electrochemical exfoliation procedure to prepare Sb nanosheets. Flakes = SbNSs and spheres = cations (*e.g.*, Na^+). (b) FE for formate (blue), CO (grey), and H_2 (orange) on the SbNS electrode at different applied potentials in 0.5 M $NaHCO_3$ solution. (c) Partial current density for formate at different applied potentials on bulk Sb (orange), SbNSs (blue), and SbNS-G (red). (d) Raman spectra of SbNSs, SbNS-G, and SbNSs mixed with exfoliated graphene (SbNS-G mix). Adapted with permission from ref. 231. Copyright 2017, Wiley-VCH Verlag GmbH & Co. KGaA.

trocatalyst for the reduction of CO_2 into CO. This material required an onset overpotential of 0.19 V for CO formation, and exhibited a lower overpotential of 0.47 V compared to that of Au and Ag at a similar FE for CO of ~85%. Systematic experiments showed that the catalytic activity was dependent on N-defect structures; pyridinic–N defects demonstrated the highest catalytic activity on lowering the free energy barrier to form the intermediate *COOH, as confirmed by DFT calculations. Similarly, our group found that pyridinic N was responsible for such ECR activity on N-doped carbon materials.[243] Tan *et al.*[244] also utilized the N-doping strategy to make graphene ECR active, but the major product in their work was formate, instead of CO. The catalyst exhibits a much lower overpotential to achieve selectivity towards the production of formate, comparable with that of many precious metal based catalysts. The authors suggested that pyridinic N, the most common N-doping mode in the catalyst, could generate significant positive charge in adjacent carbon atoms and therefore was responsible for the catalytic activity. However, DFT calculations by Zhao *et al.* showed that pyrrolic N in N-doped graphene possessed the highest catalytic activity toward the ECR among all N defects, despite the similar conclusion that N-doping could modify the electronic properties of graphene and lead to a low free energy barrier for the potential-limiting *COOH formation step.[245] Phani and coworkers studied the electrocatalytic activity of boron-doped graphene for the electroreduction of CO_2 into formate.[246] DFT calculations suggested that the presence of B in graphene resulted in an asymmetric charge and spin density, and the positive spin density on B and C atoms enabled both atoms to be catalytically active and available for chemisorption of CO_2.

3.4.3. Immobilization of homogeneous catalysts. The specific interest in "heterogenizing" homogeneous molecular catalysts by linking them to the surface of an electrode support lies in the combination of the competing advantages of homogeneous catalysts (high product selectivity and chemical structure tunability) and heterogeneous catalysts (robustness and easy separation of products from catalysts).[247] The immobilized molecular catalysts have several advantages: control over the active site environment for better performance; prevention of aggregation or dimerization of the molecular catalyst; efficient electron transfer to the molecular catalyst; usability of water-insoluble molecular catalysts in aqueous media once anchored to the electrodes; and stabilization of the catalyst and the electrode.[248–251] Immobilization of molecular catalysts onto a conductive material, such as active carbon, graphene, CNTs or indium tin oxide (ITO), can be accomplished using either non-covalent (*e.g.*, π–π interaction, electrostatic interaction) or covalent approaches. Since the first work reported in 1974 by Meshitsuka *et al.*, who utilized Ni- or Co-phthalocyanine dip-coated onto a graphite electrode to catalyze the ECR,[252] different kinds of molecular catalysts have been employed to link onto various substrates. The two-electron-transfer products, namely, CO, HCOOH, and oxalic acid ($H_2C_2O_4$), are the main products, while reports on products with more electrons transferred, such as CH_3OH and CH_4, are rare.[58]

Koper *et al.*[253] reported a Co protoporphyrin immobilized on a pyrolytic graphite electrode by a simple dip-coating method which could reduce CO_2 in an aqueous acidic solution at relatively low overpotential (0.5 V), with an efficiency and selectivity comparable to those of the best porphyrin-based electrocatalyst in the literature. While CO was the main reduction product, they also observed methane as a by-product. The major finding in their work is the pH-dependent formation of CO, which was investigated by combining cyclic voltammetry with online electrochemical mass spectrometry at different pH values. This observation suggested the formation of a $CO_2^{\bullet-}$ anion bound to the Co macrocycle, acting as a Brønsted base. This $CO_2^{\bullet-}$ anion is then protonated by water rather than by H^+, explaining why under less acidic conditions (pH = 3), CO formation can reach up to 60% FE compared to <1% at pH = 1. Further reduction of CO into CH_4 was slow with a low FE of up to 3%, and occurred through concerted

electron–proton transfer in acidic media, proposed by the authors.

Wang, Brudvig and coworkers[254] reported a molecular Cu–porphyrin complex deposited on carbon fiber paper as a heterogeneous electrocatalyst for the active and selective reduction of CO_2 into hydrocarbons (CH_4 and CH_2CH_2) in aqueous media. With a mass loading of 0.25 mg cm^{-2} and under an applied potential of −0.976 V *vs.* RHE, a partial current density of 21 mA cm^{-2} and a FE of 44% for hydrocarbons were achieved, giving turnover frequencies (TOFs) of 4.3 and 1.8 s^{-1} for CH_4 and CH_2CH_2, respectively. The catalytic performance was attributed to the Cu^I being the active center and built-in hydroxyl groups in the porphyrin structure facilitating binding of certain reaction intermediates or providing an intramolecular source of protons. Recently, Wang's group reported their work on a cobalt-phthalocyanine (CoPc) uniformly anchored on carbon nanotubes (Fig. 17a) to afford highly active and selective production of CO from CO_2 reduction in 0.1 M $KHCO_3$ aqueous solution.[255] They found that hybridization with CNTs improved not only the catalytic activity but also the product selectivity and catalytic stability (Fig. 17b). The strong interactions between the molecular complex and CNTs allowed a uniform distribution of the molecules on the highly conductive carbon support, and thus enabled a high degree of catalytic site exposure and rapid electron transfer from the electrode to surface immobilized molecules. They also found that the introduction of cyano groups into the CoPc molecule could further enhance catalytic performance, which was due to the electron-withdrawing effect, facilitating the formation of active Co^I species in the ECR.

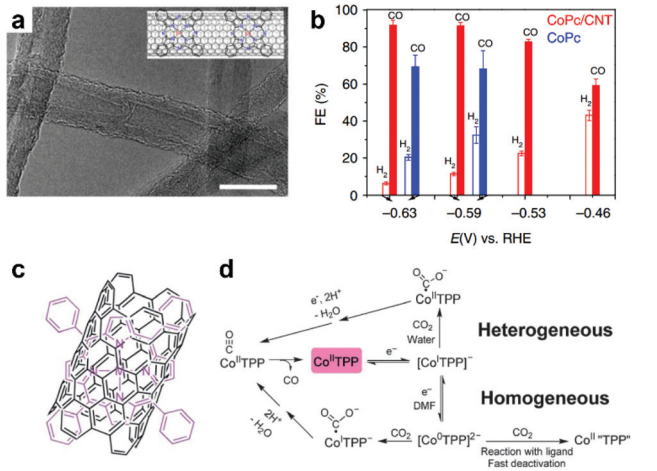

Fig. 17 (a) TEM images of the CoPc/CNT hybrid. The inset shows a schematic representation of the hybrid. (b) FEs for H_2 and CO of CoPc/CNT (red) and CoPc (blue) at various potentials. Adapted with permission from ref. 255. Copyright 2017, Nature Publishing Group. (c) Schematic illustration of the immobilized MTPP molecule on CNTs (M = Co or Fe–Cl). (d) Proposed mechanism for the ECR catalyzed by CoTPP under homogeneous and heterogeneous conditions. Adapted with permission from ref. 256. Copyright 2017, Wiley-VCH Verlag GmbH & Co. KGaA.

Daasbjerg *et al.*[256] compared the ECR on cobalt *meso*-tetraphenylporphyrin (CoTPP) under homogeneous (in an organic medium) and heterogeneous (in an aqueous medium) conditions. In the former case, CoTPP performed poorly (low activity and selectivity at a high overpotential) with Co^0 as the active center using DMF as a solvent. In contrast, straightforward immobilization of CoTPP onto carbon nanotubes (Fig. 17c) allowed the catalytic activity of this water insoluble compound to be investigated in aqueous media. A remarkable enhancement of the electrocatalytic activities was observed with Co^I being the active center and CO_2 being selectively reduced to CO (>90%) at a low overpotential in an aqueous medium. The authors ascribed this effect to the particular environment created by the aqueous medium at the catalytic site of the immobilized catalyst, which could facilitate the adsorption and further reaction of CO_2 (Fig. 17d).

4. Summary and outlook

Emissions of CO_2 from fossil fuel combustion and industrial processes have been regarded as the dominant cause of the global warming observed since the mid-20th century. Electrocatalytic reduction of CO_2 has attracted intense academic and industrial interest since it provides an effective method for the storage of intermittent energy from renewable sources in the form of chemical energy. The as-produced fuels can be used directly through a current, well-established distribution infrastructure. The stored energy can be released for end-use, such as in fuel cells, conventional fuel-burning engines or other industrial processes. Successful implementation of electrocatalytic CO_2 conversion needs catalysts that are able to catalyze the reaction in an efficient, selective and durable manner, and ideally in aqueous solution. However, this is a great challenge, which needs even greater research effort.

A number of experimental and theoretical reports have attempted to uncover the catalytic mechanisms and guide the search for novel catalysts to conquer the problems that most polycrystalline metal electrodes confront: the large overpotentials that are required to achieve appreciable current densities; poor product selectivity; and unsatisfactory stability. Recent progress has shown that nanoengineering may resolve some of these issues. In this Review, several approaches have been discussed, including tuning the size and morphology of metallic NP catalysts, forming nanoalloys with different kinds of parent metals, tuning the surface chemistry and adsorption properties of the electrocatalysts, using nanostructured metals derived from their oxides, exposing active edges site by 2D engineering of the bulk materials, constructing 3D hierarchical structures, leveraging catalysts through exploiting the support effect and heterogenizing molecular catalysts onto support electrodes. Through these methods, considerable improvements in catalytic performance have been achieved, and representative results have been summarized in Table 2.

Table 2 Representative performances of the ECR using different nanoengineering strategies

Strategy	Material	Electrolyte	Major product[a]	FE[b] (%)	η[c] (V)	Ref.
Nanosize	Au nanocluster	0.1 M $KHCO_3$	CO	~100	0.89	90
	Au NPs (8 nm)	0.5 M $KHCO_3$	CO	90	0.56	80
	Cu NPs	0.1 M $KClO_4$	C_2H_4	36	1.16	61
	Cu foil	0.1 M $KHCO_3$	CH_4	57	1.27	81
Nanomorphology	Au NWs (500 nm)	0.5 M $KHCO_3$	CO	94	0.24	97
	Triangular silver nanoplates	0.1 M $KHCO_3$	CO	96.8	0.746	98
	Cu nanocubes	0.1 M $KHCO_3$	C_2H_4	41	1.16	99
	Branched Pd NPs	0.5 M $KHCO_3$	$HCOO^-$	97	0.2	100
Nanoalloys	Core/shell Cu/SnO_2	0.5 M $KHCO_3$	$HCOO^-$	93	0.55	120
	Au–Cu alloy	0.1 M $KHCO_3$	CO	64.7	0.61	109
	Phase-separated Cu–Pd	1 M KOH[d]	C_2H_4, C_2H_5OH	63%	—	111
Oxide derivation	Oxide-derived Au	0.5 M $NaHCO_3$	CO	96	0.24	123
	Oxide-derived Cu	0.5 M $NaHCO_3$	CO	~40	0.39	122
	Oxide-derived Cu NWs	0.1 M $KHCO_3$	CO	~50	0.49	130
Surface modification	PEI-NCNTs	0.1 M $KHCO_3$	$HCOO^-$	87	1.14	153
	rGO-PEI-MoS_x	0.5 M $NaHCO_3$	CO	85.1	0.54	156
	Cysteamine anchoring Ag NPs	0.5 M $KHCO_3$	CO	84.4	0.64	87
	Carbene-functionalized Au NPs	0.1 M $KHCO_3$	CO	83	0.46	160
Support effect	Ag/TiO_2	1 M KOH[d]	CO	>95	—	170
	Au NP-CeO_x	0.1 M $KHCO_3$	CO	89.1	0.78	171
	Au NP embedded in graphene	0.5 M $KHCO_3$	CO	92	0.55	172
3D structure	Porous Ag foam	0.5 M $NaHCO_3$	CO	92	0.49	189
	Au inverse opal film	0.1 M $KHCO_3$	CO	99	0.4	182
	Cu NW	0.1 M $KHCO_3$	C_2H_4	17.4	1.16	183
	Au needles	0.5 M $KHCO_3$	CO	>95	0.24	180
2D engineering	MoS_2	H_2O/BMIM-BF_4	CO	98	0.65	225
	Partially oxidized 2D Co	0.1 M Na_2SO_4	$HCOO^-$	90.1	0.24	228
	Sb NS/graphene	0.5 M $NaHCO_3$	$HCOO^-$	88.5	0.87	231
	N-Doped graphene	0.1 M $KHCO_3$	CO	~85	0.47	239
"Heterogenizing" homogeneous catalysts	Cu-Porphyrin on carbon fiber	0.5 M $KHCO_3$	CH_4	~30	1.15	254
	CoTPP on carbon nanotubes	0.5 M $KHCO_3$	CO	91	0.55	256

[a] Product of research interest in the reference. [b] Maximum FE of the product. [c] Overpotential that achieved the maximum FE. [d] Using a flow cell.

Despite the significant effort made over the past five years, it still seems quite challenging to efficiently reduce CO_2 to products one could design and predict, especially those with more than two electrons transferred. In fact, the present development in the ECR is far below the requirements for commercial applications. Great effort is needed in the further development of this area, along several major directions.

The development of catalysts that could convert CO_2 to value added fuels and chemicals in a selective and energy efficient manner is needed. Most of the currently developed catalysts can only reduce CO_2 to the two-electron-transfer products, *i.e.*, oxalic acid, CO and formate. Although Cu is able to produce hydrocarbons and alcohols at appreciable rates, the selectivity is far from satisfactory. Novel catalysts capable of generating other high-value chemicals such as methanol from CO_2 in a highly selective and efficient way will certainly open up new opportunities.[257–259] For this, the deviation of binding energies of different intermediates (*e.g.*, *COOH, *CO, and *CHO) from the "linear relationship" is critical as suggested by DFT calculations. Some nanoengineering strategies have been proposed. For example, as highlighted above, Nørskov *et al.* have found that, on the edge of Ni-doped MoS_2, *CO bound on the doped metal site whilst *COOH and *CHO bound on the covalent S site, leading to the deviation from the scaling relationship and hence promoting the possible reduction of *CO into hydrocarbons or alcohols.[224] Through DFT calculation screening, Jung *et al.*[260] identified the W/Au alloy with a single layer of Au on top of the W substrate as a promising candidate to electroreduce CO_2 to methanol with lower overpotential and higher selectivity than conventional Cu, while suppressing the unwanted HER. Further experimental effort for verifying and exploiting these theoretical predictions are worthwhile. By introducing a suitable amount of Zn dopant into Cu-based oxides, the selectivity of CO_2 reduction toward ethanol could be tuned using this oxide-derived catalyst in aqueous media.[261] *In operando* Raman spectroscopy revealed that this Zn doped Cu-based oxide catalyst was reduced to the metallic state during catalytic turnovers and the reduction of CO_2 was likely to take place on metallic sites rather than on metal oxides. The author rationalized the observed selectivity to a two-site mechanism: Zn could catalyze the reduction of CO_2 into CO, which was further reduced to ethanol on the Cu site. Further investigations using these nanoengineering strategies are reasonably expected to bring about new findings in the production of high value chemicals from the ECR.

A better understanding of the mechanism and structure–property correlation by combining theory and experiment approaches is also needed. Despite the sustained progress made in the development of ECR catalysts, it is still not clear how CO_2 molecules are reduced on the surface of a catalyst,

which significantly restricts the further development of this catalytic reaction. A more rational optimization of the current catalysts and a further search for new catalysts require an in-depth understanding of the mechanism and structure–property correlations involved. It is expected that experimental *in situ* techniques in tandem with theoretical modeling will play an increasingly important role in the coming years as a more effective and powerful approach to the rational design of catalysts.[11] A variety of *in operando* techniques have been increasingly applied to study the ECR, although they are challenging to use. For example, the monitoring of surface species can be achieved by ATR-IR or Raman spectroscopy, as highlighted above. The composition and oxidation state of the surface can be probed by synchrotron-based ambient-pressure X-ray photoelectron spectroscopy, while the morphology and crystalline changes can be monitored by *in situ* environmental transmission electron microscopy. Due to significant advances in DFT calculations and continuously expanding computational resources, it is now possible to investigate electrocatalysts at the atomic level by computational methods. DFT calculations have been identified as a powerful tool to explain experimental results and predict new catalysts, but most of the calculations are based on oversimplified models, which limited the accuracy to some extent. Further development in optimizing theoretical calculations to take more factors into account should provide a better and more accurate understanding of the catalytic reactions.

Additionally, some other factors influencing the ECR should be considered to make this technology eventually practical. For example, the solubility of CO_2 in water is low, which will result in a low limiting current density. Therefore, the design of reactors such as gas-diffusion cells and liquid-flow cells, or the use of different media, such as solid polymer electrolytes, can be adapted to partly address this issue. Recently, ionic liquids have also been demonstrated as a promising avenue for improving the solubility of CO_2, as well as offering special stabilization of the intermediates produced in the ECR.[140,142,226,262] Other parameters such as CO_2 pressure, reaction temperature and pH, the species of electrolyte, the membrane of the electrolysis cell and anodic oxidation catalysts will also need to be considered before this technology is mature and ready for wide-scale practical applications.

Conflicts of interest

There are no conflicts to declare.

Acknowledgements

We acknowledge support from the Centre of Excellence for Electromaterials Science, Australian Research Council (ARC) through the ARC Centre of Excellence for Electromaterials Science. F. L. acknowledges the Postgraduate Publication Award from Monash University. D. R. M. is grateful to the Australian Research Council for his Australian Laureate Fellowship.

References

1 G. W. Petty, *A First Course in Atmospheric Radiation*, Sundog Pub., 2006.
2 M. Maslin, *Global Warming: a Very Short Introduction*, OUP, Oxford, 2008.
3 I. Ganesh, *Mater. Sci. Appl.*, 2011, **02**, 1407.
4 L. Cozzi and T. Gould, *World Energy Outlook 2015*, International Energy Agency, 2015.
5 C. Beer, M. Reichstein, E. Tomelleri, P. Ciais, M. Jung, N. Carvalhais, C. Rödenbeck, M. A. Arain, D. Baldocchi, G. B. Bonan, A. Bondeau, A. Cescatti, G. Lasslop, A. Lindroth, M. Lomas, S. Luyssaert, H. Margolis, K. W. Oleson, O. Roupsard, E. Veenendaal, N. Viovy, C. Williams, F. I. Woodward and D. Papale, *Science*, 2010, **329**, 834.
6 N. Nitta, F. Wu, J. T. Lee and G. Yushin, *Mater. Today*, 2015, **18**, 252.
7 G. Wang, L. Zhang and J. Zhang, *Chem. Soc. Rev.*, 2012, **41**, 797.
8 W. Wang, Q. Luo, B. Li, X. Wei, L. Li and Z. Yang, *Adv. Funct. Mater.*, 2013, **23**, 970.
9 M. Aresta, A. Dibenedetto and A. Angelini, *Chem. Rev.*, 2014, **114**, 1709.
10 D. T. Whipple and P. J. A. Kenis, *J. Phys. Chem. Lett.*, 2010, **1**, 3451.
11 Z. W. Seh, J. Kibsgaard, C. F. Dickens, I. Chorkendorff, J. K. Norskov and T. F. Jaramillo, *Science*, 2017, **355**, eaad4998.
12 A. J. Bard, R. Parsons and J. Jordan, *Standard Potentials in Aqueous Solution*, CRC Press, 1985.
13 B. P. Sullivan, K. Krist and H. Guard, *Electrochemical and Electrocatalytic Reactions of Carbon Dioxide*, Elsevier, 2012.
14 A. Aylmer-Kelly, A. Bewick, P. Cantrill and A. Tuxford, *Faraday Discuss. Chem. Soc.*, 1973, **56**, 96.
15 E. Lamy, L. Nadjo and J. Saveant, *J. Electroanal. Chem. Interfacial Electrochem.*, 1977, **78**, 403.
16 H. Schwarz and R. Dodson, *J. Phys. Chem.*, 1989, **93**, 409.
17 M. R. Dubois and D. L. Dubois, *Acc. Chem. Res.*, 2009, **42**, 9.
18 E. E. Benson, C. P. Kubiak, A. J. Sathrum and J. M. Smieja, *Chem. Soc. Rev.*, 2009, **38**, 89.
19 J. Schneider, H. Jia, J. T. Muckerman and E. Fujita, *Chem. Soc. Rev.*, 2012, **41**, 2036.
20 J. M. Saveant, *Chem. Rev.*, 2008, **108**, 2348.
21 A. M. Appel, J. E. Bercaw, A. B. Bocarsly, H. Dobbek, D. L. DuBois, M. Dupuis, J. G. Ferry, E. Fujita, R. Hille, P. J. Kenis, C. A. Kerfeld, R. H. Morris, C. H. Peden, A. R. Portis, S. W. Ragsdale, T. B. Rauchfuss, J. N. Reek, L. C. Seefeldt, R. K. Thauer and G. L. Waldrop, *Chem. Rev.*, 2013, **113**, 6621.
22 L. Zhang, Z.-J. Zhao and J. Gong, *Angew. Chem., Int. Ed.*, 2017, **56**, 11326.

23 X. Duan, J. Xu, Z. Wei, J. Ma, S. Guo, S. Wang, H. Liu and S. Dou, *Adv. Mater.*, 2017, **29**, 1701784.
24 D. D. Zhu, J. L. Liu and S. Z. Qiao, *Adv. Mater.*, 2016, **28**, 3423.
25 W. Zhang, Y. Hu, L. Ma, G. Zhu, Y. Wang, X. Xue, R. Chen, S. Yang and Z. Jin, *Adv. Sci.*, 2018, **5**, 1700275.
26 J. Qiao, Y. Liu, F. Hong and J. Zhang, *Chem. Soc. Rev.*, 2014, **43**, 631.
27 Q. Lu, J. Rosen and F. Jiao, *ChemCatChem*, 2015, **7**, 38.
28 J.-P. Jones, G. K. S. Prakash and G. A. Olah, *Isr. J. Chem.*, 2014, **54**, 1451.
29 Q. Lu and F. Jiao, *Nano Energy*, 2016, **29**, 439.
30 Z.-L. Wang, C. Li and Y. Yamauchi, *Nano Today*, 2016, **11**, 373.
31 G. O. Larrazabal, A. J. Martin and J. Perez-Ramirez, *J. Phys. Chem. Lett.*, 2017, **8**, 3933.
32 D. Voiry, J. Yang and M. Chhowalla, *Adv. Mater.*, 2016, **28**, 6197.
33 X. Zou and Y. Zhang, *Chem. Soc. Rev.*, 2015, **44**, 5148.
34 C. Tang and Q. Zhang, *Adv. Mater.*, 2017, **29**, 1604103.
35 W. Xia, A. Mahmood, Z. Liang, R. Zou and S. Guo, *Angew. Chem., Int. Ed.*, 2016, **55**, 2650.
36 M. Shao, Q. Chang, J. P. Dodelet and R. Chenitz, *Chem. Rev.*, 2016, **116**, 3594.
37 Y. Nie, L. Li and Z. Wei, *Chem. Soc. Rev.*, 2015, **44**, 2168.
38 B. Braunchweig, D. Hibbitts, M. Neurock and A. Wieckowski, *Catal. Today*, 2013, **202**, 197.
39 K. Udupa, G. Subramanian and H. Udupa, *Electrochim. Acta*, 1971, **16**, 1593.
40 S. Kapusta, *J. Electrochem. Soc.*, 1983, **130**, 607.
41 Y. Hori, H. Wakebe, T. Tsukamoto and O. Koga, *Electrochim. Acta*, 1994, **39**, 1833.
42 M. Jitaru, D. Lowy, M. Toma, B. Toma and L. Oniciu, *J. Appl. Electrochem.*, 1997, **27**, 875.
43 N. Hoshi, M. Kato and Y. Hori, *J. Electroanal. Chem.*, 1997, **440**, 283.
44 Y. Hori, A. Murata, K. Kikuchi and S. Suzuki, *J. Chem. Soc., Chem. Commun.*, 1987, 728.
45 Y. Hori, R. Takahashi, Y. Yoshinami and A. Murata, *J. Phys. Chem. B*, 1997, **101**, 7075.
46 K. P. Kuhl, T. Hatsukade, E. R. Cave, D. N. Abram, J. Kibsgaard and T. F. Jaramillo, *J. Am. Chem. Soc.*, 2014, **136**, 14107.
47 Y. Hori, in *Modern Aspects of Electrochemistry*, ed. C. G. Vayenas, R. E. White and M. E. Gamboa-Aldeco, Springer, New York, 2008, vol. 42, p. 89.
48 Y. Hori, in *Solar to Chemical Energy Conversion*, Springer, 2016, p. 191.
49 A. A. Peterson, F. Abild-Pedersen, F. Studt, J. Rossmeisl and J. K. Nørskov, *Energy Environ. Sci.*, 2010, **3**, 1311.
50 A. A. Peterson and J. K. Nørskov, *J. Phys. Chem. Lett.*, 2012, **3**, 251.
51 H. A. Hansen, J. B. Varley, A. A. Peterson and J. K. Norskov, *J. Phys. Chem. Lett.*, 2013, **4**, 388.
52 C. Shi, H. A. Hansen, A. C. Lausche and J. K. Norskov, *Phys. Chem. Chem. Phys.*, 2014, **16**, 4720.
53 Z. P. Jovanov, H. A. Hansen, A. S. Varela, P. Malacrida, A. A. Peterson, J. K. Nørskov, I. E. L. Stephens and I. Chorkendorff, *J. Catal.*, 2016, **343**, 215.
54 C. Shi, K. Chan, J. S. Yoo and J. K. Nørskov, *Org. Process Res. Dev.*, 2016, **20**, 1424.
55 J. S. Yoo, R. Christensen, T. Vegge, J. K. Norskov and F. Studt, *ChemSusChem*, 2016, **9**, 358.
56 J. T. Feaster, C. Shi, E. R. Cave, T. Hatsukade, D. N. Abram, K. P. Kuhl, C. Hahn, J. K. Nørskov and T. F. Jaramillo, *ACS Catal.*, 2017, 4822, DOI: 10.1021/acscatal.7b00687.
57 F. Calle-Vallejo and M. T. Koper, *Angew. Chem., Int. Ed.*, 2013, **52**, 7282.
58 R. Kortlever, J. Shen, K. J. Schouten, F. Calle-Vallejo and M. T. Koper, *J. Phys. Chem. Lett.*, 2015, **6**, 4073.
59 H. Ooka, M. C. Figueiredo and M. T. M. Koper, *Langmuir*, 2017, **33**, 9307.
60 K. P. Kuhl, E. R. Cave, D. N. Abram and T. F. Jaramillo, *Energy Environ. Sci.*, 2012, **5**, 7050.
61 W. Tang, A. A. Peterson, A. S. Varela, Z. P. Jovanov, L. Bech, W. J. Durand, S. Dahl, J. K. Norskov and I. Chorkendorff, *Phys. Chem. Chem. Phys.*, 2012, **14**, 76.
62 J. Xiao and T. Frauenheim, *J. Phys. Chem. C*, 2013, **117**, 1804.
63 M. F. Baruch, J. E. Pander, J. L. White and A. B. Bocarsly, *ACS Catal.*, 2015, **5**, 3148.
64 A. Dutta, A. Kuzume, M. Rahaman, S. Vesztergom and P. Broekmann, *ACS Catal.*, 2015, **5**, 7498.
65 R. Kas, R. Kortlever, H. Yılmaz, M. T. M. Koper and G. Mul, *ChemElectroChem*, 2015, **2**, 354.
66 Y. Li, S. H. Chan and Q. Sun, *Nanoscale*, 2015, **7**, 8663.
67 Y. Li and Q. Sun, *Adv. Energy Mater.*, 2016, **6**, 1600463.
68 M. Dunwell, Q. Lu, J. M. Heyes, J. Rosen, J. G. Chen, Y. Yan, F. Jiao and B. Xu, *J. Am. Chem. Soc.*, 2017, **139**, 3774.
69 N. J. Firet and W. A. Smith, *ACS Catal.*, 2017, **7**, 606.
70 S. Back, M. S. Yeom and Y. Jung, *ACS Catal.*, 2015, **5**, 5089.
71 M. Gattrell, N. Gupta and A. Co, *J. Electroanal. Chem.*, 2006, **594**, 1.
72 R. Schlögl, *Angew. Chem., Int. Ed.*, 2015, **54**, 3465.
73 R. Chaplin and A. Wragg, *J. Appl. Electrochem.*, 2003, **33**, 1107.
74 H. Noda, S. Ikeda, A. Yamamoto, H. Einaga and K. Ito, *Bull. Chem. Soc. Jpn.*, 1995, **68**, 1889.
75 H. Mistry, A. S. Varela, S. Kühl, P. Strasser and B. R. Cuenya, *Nat. Rev. Mater.*, 2016, **1**, 16009.
76 T. Bligaard and J. K. Nørskov, *Electrochim. Acta*, 2007, **52**, 5512.
77 D. Astruc, *Nanoparticles and Catalysis*, John Wiley & Sons, 2008.
78 A. Wieckowski, E. R. Savinova and C. G. Vayenas, *Catalysis and Electrocatalysis at Nanoparticle Surfaces*, CRC Press, 2003.

79 C. M. Welch and R. G. Compton, *Anal. Bioanal. Chem.*, 2006, **384**, 601.
80 W. Zhu, R. Michalsky, O. Metin, H. Lv, S. Guo, C. J. Wright, X. Sun, A. A. Peterson and S. Sun, *J. Am. Chem. Soc.*, 2013, **135**, 16833.
81 R. Reske, H. Mistry, F. Behafarid, B. Roldan Cuenya and P. Strasser, *J. Am. Chem. Soc.*, 2014, **136**, 6978.
82 H. Mistry, R. Reske, Z. Zeng, Z. J. Zhao, J. Greeley, P. Strasser and B. R. Cuenya, *J. Am. Chem. Soc.*, 2014, **136**, 16473.
83 K. Manthiram, B. J. Beberwyck and A. P. Alivisatos, *J. Am. Chem. Soc.*, 2014, **136**, 13319.
84 D. Gao, H. Zhou, J. Wang, S. Miao, F. Yang, G. Wang, J. Wang and X. Bao, *J. Am. Chem. Soc.*, 2015, **137**, 4288.
85 Z. Zhang, M. Chi, G. M. Veith, P. Zhang, D. A. Lutterman, J. Rosenthal, S. H. Overbury, S. Dai and H. Zhu, *ACS Catal.*, 2016, **6**, 6255.
86 S. Zhang, P. Kang and T. J. Meyer, *J. Am. Chem. Soc.*, 2014, **136**, 1734.
87 C. Kim, H. S. Jeon, T. Eom, M. S. Jee, H. Kim, C. M. Friend, B. K. Min and Y. J. Hwang, *J. Am. Chem. Soc.*, 2015, **137**, 13844.
88 H. Zhang, G. Liu, L. Shi and J. Ye, *Adv. Energy Mater.*, 2018, **8**, 1701343.
89 X. F. Yang, A. Wang, B. Qiao, J. Li, J. Liu and T. Zhang, *Acc. Chem. Res.*, 2013, **46**, 1740.
90 D. R. Kauffman, D. Alfonso, C. Matranga, H. Qian and R. Jin, *J. Am. Chem. Soc.*, 2012, **134**, 10237.
91 D. R. Kauffman, D. Alfonso, C. Matranga, P. Ohodnicki, X. Deng, R. C. Siva, C. Zeng and R. Jin, *Chem. Sci.*, 2014, **5**, 3151.
92 S. X. Guo, D. R. MacFarlane and J. Zhang, *ChemSusChem*, 2016, **9**, 80.
93 C. Zhao, X. Dai, T. Yao, W. Chen, X. Wang, J. Wang, J. Yang, S. Wei, Y. Wu and Y. Li, *J. Am. Chem. Soc.*, 2017, **139**, 8078.
94 X. Li, W. Bi, M. Chen, Y. Sun, H. Ju, W. Yan, J. Zhu, X. Wu, W. Chu, C. Wu and Y. Xie, *J. Am. Chem. Soc.*, 2017, **139**, 14889.
95 K. Jiang, S. Siahrostami, A. J. Akey, Y. Li, Z. Lu, J. Lattimer, Y. Hu, C. Stokes, M. Gangishetty, G. Chen, Y. Zhou, W. Hill, W.-B. Cai, D. Bell, K. Chan, J. K. Nørskov, Y. Cui and H. Wang, *Chem*, 2017, **3**, 950.
96 X. Wang, Z. Chen, X. Zhao, T. Yao, W. Chen, R. You, C. Zhao, G. Wu, J. Wang, W. Huang, J. Yang, X. Hong, S. Wei, Y. Wu and Y. Li, *Angew. Chem., Int. Ed.*, 2018, **57**, 1944.
97 W. Zhu, Y. J. Zhang, H. Zhang, H. Lv, Q. Li, R. Michalsky, A. A. Peterson and S. Sun, *J. Am. Chem. Soc.*, 2014, **136**, 16132.
98 S. Liu, H. Tao, L. Zeng, Q. Liu, Z. Xu, Q. Liu and J. L. Luo, *J. Am. Chem. Soc.*, 2017, **139**, 2160.
99 A. Loiudice, P. Lobaccaro, E. A. Kamali, T. Thao, B. H. Huang, J. W. Ager and R. Buonsanti, *Angew. Chem., Int. Ed.*, 2016, **55**, 5789.
100 A. Klinkova, P. D. Luna, C.-T. Dinh, O. Voznyy, E. M. Larin, E. Kumacheva and E. H. Sargent, *ACS Catal.*, 2016, **6**, 8115.
101 R. Kortlever, I. Peters, C. Balemans, R. Kas, Y. Kwon, G. Mul and M. T. Koper, *Chem. Commun.*, 2016, **52**, 10229.
102 D. A. Torelli, S. A. Francis, J. C. Crompton, A. Javier, J. R. Thompson, B. S. Brunschwig, M. P. Soriaga and N. S. Lewis, *ACS Catal.*, 2016, **6**, 2100.
103 C. Hahn, D. N. Abram, H. A. Hansen, T. Hatsukade, A. Jackson, N. C. Johnson, T. R. Hellstern, K. P. Kuhl, E. R. Cave, J. T. Feaster and T. F. Jaramillo, *J. Mater. Chem. A*, 2015, **3**, 20185.
104 X. Bai, W. Chen, C. Zhao, S. Li, Y. Song, R. Ge, W. Wei and Y. Sun, *Angew. Chem., Int. Ed.*, 2017, **56**, 12219.
105 S. Zhang, P. Kang, M. Bakir, A. M. Lapides, C. J. Dares and T. J. Meyer, *Proc. Natl. Acad. Sci. U. S. A.*, 2015, **112**, 15809.
106 S. Rasul, D. H. Anjum, A. Jedidi, Y. Minenkov, L. Cavallo and K. Takanabe, *Angew. Chem., Int. Ed.*, 2015, **54**, 2146.
107 S. Sarfraz, A. T. Garcia-Esparza, A. Jedidi, L. Cavallo and K. Takanabe, *ACS Catal.*, 2016, **6**, 2842.
108 Y. Zhao, C. Wang and G. G. Wallace, *J. Mater. Chem. A*, 2016, **4**, 10710.
109 D. Kim, J. Resasco, Y. Yu, A. M. Asiri and P. Yang, *Nat. Commun.*, 2014, **5**, 4948.
110 D. Kim, C. Xie, N. Becknell, Y. Yu, M. Karamad, K. Chan, E. J. Crumlin, J. K. Norskov and P. Yang, *J. Am. Chem. Soc.*, 2017, **139**, 8329.
111 S. Ma, M. Sadakiyo, M. Heima, R. Luo, R. T. Haasch, J. I. Gold, M. Yamauchi and P. J. Kenis, *J. Am. Chem. Soc.*, 2017, **139**, 47.
112 J. R. Kitchin, J. K. Nørskov, M. A. Barteau and J. Chen, *Phys. Rev. Lett.*, 2004, **93**, 156801.
113 P. Strasser, S. Koh, T. Anniyev, J. Greeley, K. More, C. Yu, Z. Liu, S. Kaya, D. Nordlund and H. Ogasawara, *Nat. Chem.*, 2010, **2**, 454.
114 D. Plana, J. Flórez-Montano, V. Celorrio, E. Pastor and D. J. Fermín, *Chem. Commun.*, 2013, **49**, 10962.
115 A. S. Varela, C. Schlaup, Z. P. Jovanov, P. Malacrida, S. Horch, I. E. Stephens and I. Chorkendorff, *J. Phys. Chem. C*, 2013, **117**, 20500.
116 R. Reske, M. Duca, M. Oezaslan, K. J. P. Schouten, M. T. Koper and P. Strasser, *J. Phys. Chem. Lett.*, 2013, **4**, 2410.
117 J. Monzó, Y. Malewski, R. Kortlever, F. J. Vidal-Iglesias, J. Solla-Gullón, M. T. M. Koper and P. Rodriguez, *J. Mater. Chem. A*, 2015, **3**, 23690.
118 T. Adit Maark and B. R. K. Nanda, *J. Phys. Chem. C*, 2017, **121**, 4496.
119 M. B. Ross, C. T. Dinh, Y. Li, D. Kim, P. De Luna, E. H. Sargent and P. Yang, *J. Am. Chem. Soc.*, 2017, **139**, 9359.
120 Q. Li, J. Fu, W. Zhu, Z. Chen, B. Shen, L. Wu, Z. Xi, T. Wang, G. Lu, J. J. Zhu and S. Sun, *J. Am. Chem. Soc.*, 2017, **139**, 4290.
121 W. Luc, C. Collins, S. Wang, H. Xin, K. He, Y. Kang and F. Jiao, *J. Am. Chem. Soc.*, 2017, **139**, 1885.
122 C. W. Li and M. W. Kanan, *J. Am. Chem. Soc.*, 2012, **134**, 7231.

123 Y. Chen, C. W. Li and M. W. Kanan, *J. Am. Chem. Soc.*, 2012, **134**, 19969.
124 S. Wang, J. Lin and X. Wang, *Phys. Chem. Chem. Phys.*, 2014, **16**, 14656.
125 A. Verdaguer-Casadevall, C. W. Li, T. P. Johansson, S. B. Scott, J. T. McKeown, M. Kumar, I. E. Stephens, M. W. Kanan and I. Chorkendorff, *J. Am. Chem. Soc.*, 2015, **137**, 9808.
126 X. Feng, K. Jiang, S. Fan and M. W. Kanan, *ACS Cent. Sci.*, 2016, **2**, 169.
127 A. Eilert, F. Cavalca, F. S. Roberts, J. Osterwalder, C. Liu, M. Favaro, E. J. Crumlin, H. Ogasawara, D. Friebel, L. G. Pettersson and A. Nilsson, *J. Phys. Chem. Lett.*, 2017, **8**, 285.
128 R. Kas, R. Kortlever, A. Milbrat, M. T. Koper, G. Mul and J. Baltrusaitis, *Phys. Chem. Chem. Phys.*, 2014, **16**, 12194.
129 D. Ren, Y. Deng, A. D. Handoko, C. S. Chen, S. Malkhandi and B. S. Yeo, *ACS Catal.*, 2015, **5**, 2814.
130 M. Ma, K. Djanashvili and W. A. Smith, *Phys. Chem. Chem. Phys.*, 2015, **17**, 20861.
131 C. H. Lee and M. W. Kanan, *ACS Catal.*, 2015, **5**, 465.
132 Y. Chen and M. W. Kanan, *J. Am. Chem. Soc.*, 2012, **134**, 1986.
133 X. Feng, K. Jiang, S. Fan and M. W. Kanan, *J. Am. Chem. Soc.*, 2015, **137**, 4606.
134 Z. M. Detweiler, J. L. White, S. L. Bernasek and A. B. Bocarsly, *Langmuir*, 2014, **30**, 7593.
135 C. Cui, J. Han, X. Zhu, X. Liu, H. Wang, D. Mei and Q. Ge, *J. Catal.*, 2016, **343**, 257.
136 A. Murata and Y. Hori, *Bull. Chem. Soc. Jpn.*, 1991, **64**, 123.
137 Y. Hori, A. Murata and R. Takahashi, *J. Chem. Soc., Faraday Trans.*, 1989, **85**, 2309.
138 M. R. Singh, Y. Kwon, Y. Lum, J. W. I. Ager and A. T. Bell, *J. Am. Chem. Soc.*, 2016, **138**, 13006.
139 A. S. Varela, W. Ju, T. Reier and P. Strasser, *ACS Catal.*, 2016, **6**, 2136.
140 B. A. Rosen, A. Salehi-Khojin, M. R. Thorson, W. Zhu, D. T. Whipple, P. J. Kenis and R. I. Masel, *Science*, 2011, **334**, 643.
141 J. Resasco, L. D. Chen, E. Clark, C. Tsai, C. Hahn, T. F. Jaramillo, K. Chan and A. T. Bell, *J. Am. Chem. Soc.*, 2017, **139**, 11277.
142 G. P. Lau, M. Schreier, D. Vasilyev, R. Scopelliti, M. Gratzel and P. J. Dyson, *J. Am. Chem. Soc.*, 2016, **138**, 7820.
143 S. Ponnurangam, I. V. Chernyshova and P. Somasundaran, *Adv. Colloid Interface Sci.*, 2016, **244**, 184.
144 D. Gao, F. Scholten and B. Roldan Cuenya, *ACS Catal.*, 2017, **7**, 5112.
145 S. Lee, D. Kim and J. Lee, *Angew. Chem., Int. Ed.*, 2015, **54**, 14701.
146 F. Quan, M. Xiong, F. Jia and L. Zhang, *Appl. Surf. Sci.*, 2017, **399**, 48.
147 L.-Y. Gan and Y.-J. Zhao, *J. Chem. Phys.*, 2010, **133**, 094703.
148 K. Hara, A. Tsuneto, A. Kudo and T. Sakata, *J. Electroanal. Chem.*, 1997, **434**, 239.
149 E. E. L. Tanner, C. Batchelor-McAuley and R. G. Compton, *J. Phys. Chem. C*, 2016, **120**, 26442.
150 L. Chen, S.-X. Guo, F. Li, C. Bentley, M. Horne, A. M. Bond and J. Zhang, *ChemSusChem*, 2016, **9**, 1271.
151 L. Chen, F. Li, C. L. Bentley, M. Horne, A. M. Bond and J. Zhang, *ChemElectroChem*, 2017, **4**, 1402.
152 L. Chen, F. Li, Y. Zhang, C. L. Bentley, M. Horne, A. M. Bond and J. Zhang, *ChemSusChem*, 2017, **10**, 4109.
153 S. Zhang, P. Kang, S. Ubnoske, M. K. Brennaman, N. Song, R. L. House, J. T. Glass and T. J. Meyer, *J. Am. Chem. Soc.*, 2014, **136**, 7845.
154 S. Wang, D. Yu, L. Dai, D. W. Chang and J. B. Baek, *ACS Nano*, 2011, **5**, 6202.
155 S. Wang, D. Yu and L. Dai, *J. Am. Chem. Soc.*, 2011, **133**, 5182.
156 F. Li, S.-F. Zhao, L. Chen, A. Khan, D. R. MacFarlane and J. Zhang, *Energy Environ. Sci.*, 2016, **9**, 216.
157 A. Salehi-Khojin, H.-R. M. Jhong, B. A. Rosen, W. Zhu, S. Ma, P. J. Kenis and R. I. Masel, *J. Phys. Chem. C*, 2013, **117**, 1627.
158 H. K. Lim, H. Shin, W. A. Goddard 3rd, Y. J. Hwang, B. K. Min and H. Kim, *J. Am. Chem. Soc.*, 2014, **136**, 11355.
159 C. Kim, T. Eom, M. S. Jee, H. Jung, H. Kim, B. K. Min and Y. J. Hwang, *ACS Catal.*, 2017, **7**, 779.
160 Z. Cao, D. Kim, D. Hong, Y. Yu, J. Xu, S. Lin, X. Wen, E. M. Nichols, K. Jeong, J. A. Reimer, P. Yang and C. J. Chang, *J. Am. Chem. Soc.*, 2016, **138**, 8120.
161 M. S. Xie, B. Y. Xia, Y. Li, Y. Yan, Y. Yang, Q. Sun, S. H. Chan, A. Fisher and X. Wang, *Energy Environ. Sci.*, 2016, **9**, 1687.
162 B. E. Hayden, *Acc. Chem. Res.*, 2013, **46**, 1858.
163 S. Kattel, P. Liu and J. G. Chen, *J. Am. Chem. Soc.*, 2017, **139**, 9739.
164 F. Li, L. Chen, M. Xue, T. Williams, Y. Zhang, D. R. MacFarlane and J. Zhang, *Nano Energy*, 2017, **31**, 270.
165 Q. Fu, W.-X. Li, Y. Yao, H. Liu, H.-Y. Su, D. Ma, X.-K. Gu, L. Chen, Z. Wang and H. Zhang, *Science*, 2010, **328**, 1141.
166 J. A. Rodríguez, S. Ma, P. Liu, J. Hrbek, J. Evans and M. Perez, *Science*, 2007, **318**, 1757.
167 J. Graciani, K. Mudiyanselage, F. Xu, A. E. Baber, J. Evans, S. D. Senanayake, D. J. Stacchiola, P. Liu, J. Hrbek and J. F. Sanz, *Science*, 2014, **345**, 546.
168 S. Li, Y. Xu, Y. Chen, W. Li, L. Lin, M. Li, Y. Deng, X. Wang, B. Ge, C. Yang, S. Yao, J. Xie, Y. Li, X. Liu and D. Ma, *Angew. Chem., Int. Ed.*, 2017, **56**, 10761.
169 A. Kowal, M. Li, M. Shao, K. Sasaki, M. B. Vukmirovic, J. Zhang, N. S. Marinkovic, P. Liu, A. I. Frenkel and R. R. Adzic, *Nat. Mater.*, 2009, **8**, 325.
170 S. Ma, Y. Lan, G. M. Perez, S. Moniri and P. J. Kenis, *ChemSusChem*, 2014, **7**, 866.
171 D. Gao, Y. Zhang, Z. Zhou, F. Cai, X. Zhao, W. Huang, Y. Li, J. Zhu, P. Liu, F. Yang, G. Wang and X. Bao, *J. Am. Chem. Soc.*, 2017, **139**, 5652.

172 C. Rogers, W. S. Perkins, G. Veber, T. E. Williams, R. R. Cloke and F. R. Fischer, *J. Am. Chem. Soc.*, 2017, **139**, 4052.
173 X. Lu, T. H. Tan, Y. H. Ng and R. Amal, *Chem. – Eur. J.*, 2016, **22**, 11991.
174 Y. Li, H. Su, S. H. Chan and Q. Sun, *ACS Catal.*, 2015, **5**, 6658.
175 P. Trogadas, V. Ramani, P. Strasser, T. F. Fuller and M. O. Coppens, *Angew. Chem., Int. Ed.*, 2016, **55**, 122.
176 J. Lai, S. Li, F. Wu, M. Saqib, R. Luque and G. Xu, *Energy Environ. Sci.*, 2016, **9**, 1210.
177 J. Miao, F. X. Xiao, H. B. Yang, S. Y. Khoo, J. Chen, Z. Fan, Y. Y. Hsu, H. M. Chen, H. Zhang and B. Liu, *Sci. Adv.*, 2015, **1**, e1500259.
178 F. Li, L. Chen, G. P. Knowles, D. R. MacFarlane and J. Zhang, *Angew. Chem., Int. Ed.*, 2017, **56**, 505.
179 T. Saberi Safaei, A. Mepham, X. Zheng, Y. Pang, C. T. Dinh, M. Liu, D. Sinton, S. O. Kelley and E. H. Sargent, *Nano Lett.*, 2016, **16**, 7224.
180 M. Liu, Y. Pang, B. Zhang, P. De Luna, O. Voznyy, J. Xu, X. Zheng, C. T. Dinh, F. Fan, C. Cao, F. P. de Arquer, T. S. Safaei, A. Mepham, A. Klinkova, E. Kumacheva, T. Filleter, D. Sinton, S. O. Kelley and E. H. Sargent, *Nature*, 2016, **537**, 382.
181 Y. Yoon, A. S. Hall and Y. Surendranath, *Angew. Chem.*, 2016, **128**, 15508.
182 A. S. Hall, Y. Yoon, A. Wuttig and Y. Surendranath, *J. Am. Chem. Soc.*, 2015, **137**, 14834.
183 M. Ma, K. Djanashvili and W. A. Smith, *Angew. Chem., Int. Ed.*, 2016, **55**, 6680.
184 R. Daiyan, X. Lu, Y. H. Ng and R. Amal, *ChemistrySelect*, 2017, **2**, 879.
185 D. Du, R. Lan, J. Humphreys, S. Sengodan, K. Xie, H. Wang and S. Tao, *ChemistrySelect*, 2016, **1**, 1711.
186 H. Won da, C. H. Choi, J. Chung, M. W. Chung, E. H. Kim and S. I. Woo, *ChemSusChem*, 2015, **8**, 3092.
187 F. Zhou, H. Li, M. Fournier and D. R. MacFarlane, *ChemSusChem*, 2017, **10**, 1509.
188 R. Kas, K. K. Hummadi, R. Kortlever, P. de Wit, A. Milbrat, M. W. Luiten-Olieman, N. E. Benes, M. T. Koper and G. Mul, *Nat. Commun.*, 2016, **7**, 10748.
189 Q. Lu, J. Rosen, Y. Zhou, G. S. Hutchings, Y. C. Kimmel, J. G. Chen and F. Jiao, *Nat. Commun.*, 2014, **5**, 3242.
190 J. Rosen, G. S. Hutchings, Q. Lu, S. Rivera, Y. Zhou, D. G. Vlachos and F. Jiao, *ACS Catal.*, 2015, **5**, 4293.
191 D. Raciti, K. J. Livi and C. Wang, *Nano Lett.*, 2015, **15**, 6829.
192 K. D. Yang, W. R. Ko, J. H. Lee, S. J. Kim, H. Lee, M. H. Lee and K. T. Nam, *Angew. Chem., Int. Ed.*, 2017, **56**, 796.
193 T. Burdyny, P. J. Graham, Y. Pang, C.-T. Dinh, M. Liu, E. H. Sargent and D. Sinton, *ACS Sustainable Chem. Eng.*, 2017, **5**, 4031.
194 Z. Lin, A. McCreary, N. Briggs, S. Subramanian, K. Zhang, Y. Sun, X. Li, N. J. Borys, H. Yuan, S. K. Fullerton-Shirey, A. Chernikov, H. Zhao, S. McDonnell, A. M. Lindenberg, K. Xiao, B. J. LeRoy, M. Drndić, J. C. M. Hwang, J. Park, M. Chhowalla, R. E. Schaak, A. Javey, M. C. Hersam, J. Robinson and M. Terrones, *2D Mater.*, 2016, **3**, 042001.
195 F. Bonaccorso, L. Colombo, G. Yu, M. Stoller, V. Tozzini, A. C. Ferrari, R. S. Ruoff and V. Pellegrini, *Science*, 2015, **347**, 1246501.
196 B. Anasori, M. R. Lukatskaya and Y. Gogotsi, *Nat. Rev. Mater.*, 2017, **2**, 16098.
197 M. Pumera and Z. Sofer, *Adv. Mater.*, 2017, **29**, 1605299.
198 Q. Lu, Y. Yu, Q. Ma, B. Chen and H. Zhang, *Adv. Mater.*, 2016, **28**, 1917.
199 R. Lv, J. A. Robinson, R. E. Schaak, D. Sun, Y. Sun, T. E. Mallouk and M. Terrones, *Acc. Chem. Res.*, 2015, **48**, 56.
200 R. Ma and T. Sasaki, *Acc. Chem. Res.*, 2015, **48**, 136.
201 Y. Sun, S. Gao, F. Lei, C. Xiao and Y. Xie, *Acc. Chem. Res.*, 2015, **48**, 3.
202 M. Nasilowski, B. Mahler, E. Lhuillier, S. Ithurria and B. Dubertret, *Chem. Rev.*, 2016, **116**, 10934.
203 M. Xu, T. Liang, M. Shi and H. Chen, *Chem. Rev.*, 2013, **113**, 3766.
204 M. Chhowalla, Z. Liu and H. Zhang, *Chem. Soc. Rev.*, 2015, **44**, 2584.
205 X. Duan, C. Wang, A. Pan, R. Yu and X. Duan, *Chem. Soc. Rev.*, 2015, **44**, 8859.
206 X. Kong, Q. Liu, C. Zhang, Z. Peng and Q. Chen, *Chem. Soc. Rev.*, 2017, **46**, 2127.
207 Y. Shi, H. Li and L. J. Li, *Chem. Soc. Rev.*, 2015, **44**, 2744.
208 Y. Sun, S. Gao, F. Lei and Y. Xie, *Chem. Soc. Rev.*, 2015, **44**, 623.
209 C. Tan and H. Zhang, *Chem. Soc. Rev.*, 2015, **44**, 2713.
210 H. Wang, H. Yuan, S. Sae Hong, Y. Li and Y. Cui, *Chem. Soc. Rev.*, 2015, **44**, 2664.
211 X. Wang, G. Sun, P. Routh, D. H. Kim, W. Huang and P. Chen, *Chem. Soc. Rev.*, 2014, **43**, 7067.
212 M. Chhowalla, H. S. Shin, G. Eda, L. J. Li, K. P. Loh and H. Zhang, *Nat. Chem.*, 2013, **5**, 263.
213 D. Deng, K. S. Novoselov, Q. Fu, N. Zheng, Z. Tian and X. Bao, *Nat. Nanotechnol.*, 2016, **11**, 218.
214 E. Pomerantseva and Y. Gogotsi, *Nat. Energy*, 2017, **2**, 17089.
215 A. J. Mannix, B. Kiraly, M. C. Hersam and N. P. Guisinger, *Nat. Rev. Chem.*, 2017, **1**, 0014.
216 F. Li, M. Xue, J. Li, X. Ma, L. Chen, X. Zhang, D. MacFarlane and J. Zhang, *Angew. Chem., Int. Ed.*, 2017, **56**, 14718.
217 J. D. Benck, T. R. Hellstern, J. Kibsgaard, P. Chakthranont and T. F. Jaramillo, *ACS Catal.*, 2014, **4**, 3957.
218 Y. Li, H. Wang, L. Xie, Y. Liang, G. Hong and H. Dai, *J. Am. Chem. Soc.*, 2011, **133**, 7296.
219 P. G. M. Berit Hinnemann, J. Bonde, K. P. Jørgensen, J. H. Nielsen, S. Horch, Ib Chorkendorff and J. K. Nørskov, *J. Am. Chem. Soc.*, 2005, **15**, 2.
220 G. Li, D. Zhang, Q. Qiao, Y. Yu, D. Peterson, A. Zafar, R. Kumar, S. Curtarolo, F. Hunte, S. Shannon, Y. Zhu, W. Yang and L. Cao, *J. Am. Chem. Soc.*, 2016, **138**, 16632.

221 T. F. Jaramillo, K. P. Jorgensen, J. Bonde, J. H. Nielsen, S. Horch and I. Chorkendorff, *Science*, 2007, **317**, 100.
222 K. Chan, C. Tsai, H. A. Hansen and J. K. Nørskov, *ChemCatChem*, 2014, **6**, 1899.
223 C. Tsai, K. Chan, J. K. Nørskov and F. Abild-Pedersen, *Catal. Sci. Technol.*, 2015, **5**, 246.
224 X. Hong, K. Chan, C. Tsai and J. K. Nørskov, *ACS Catal.*, 2016, **6**, 4428.
225 M. Asadi, B. Kumar, A. Behranginia, B. A. Rosen, A. Baskin, N. Repnin, D. Pisasale, P. Phillips, W. Zhu, R. Haasch, R. F. Klie, P. Kral, J. Abiade and A. Salehi-Khojin, *Nat. Commun.*, 2014, **5**, 4470.
226 M. Asadi, K. Kim, C. Liu, A. V. Addepalli, P. Abbasi, P. Yasaei, P. Phillips, A. Behranginia, J. M. Cerrato, R. Haasch, P. Zapol, B. Kumar, R. F. Klie, J. Abiade, L. A. Curtiss and A. Salehi-Khojin, *Science*, 2016, **353**, 467.
227 Y. Sun, J. Xu, X. Li, W. Liu, Z. Ju, T. Yao, C. Wang, H. Ju, J. Zhu, S. Wei and Y. Xie, *Angew. Chem., Int. Ed.*, 2017, **56**, 9121.
228 S. Gao, Y. Lin, X. Jiao, Y. Sun, Q. Luo, W. Zhang, D. Li, J. Yang and Y. Xie, *Nature*, 2016, **529**, 68.
229 S. Gao, Z. Sun, W. Liu, X. Jiao, X. Zu, Q. Hu, Y. Sun, T. Yao, W. Zhang, S. Wei and Y. Xie, *Nat. Commun.*, 2017, **8**, 14503.
230 S. Gao, X. Jiao, Z. Sun, W. Zhang, Y. Sun, C. Wang, Q. Hu, X. Zu, F. Yang, S. Yang, L. Liang, J. Wu and Y. Xie, *Angew. Chem., Int. Ed.*, 2016, **55**, 698.
231 F. Li, M. Xue, J. Li, X. Ma, L. Chen, X. Zhang, D. R. MacFarlane and J. Zhang, *Angew. Chem., Int. Ed.*, 2017, **56**, 14718.
232 J. Duan, S. Chen, M. Jaroniec and S. Z. Qiao, *ACS Catal.*, 2015, **5**, 5207.
233 Z. Yang, Z. Yao, G. Li, G. Fang, H. Nie, Z. Liu, X. Zhou, X. Chen and S. Huang, *ACS Nano*, 2012, **6**, 205.
234 C. Zhang, N. Mahmood, H. Yin, F. Liu and Y. Hou, *Adv. Mater.*, 2013, **25**, 4932.
235 J. Liang, Y. Jiao, M. Jaroniec and S. Z. Qiao, *Angew. Chem., Int. Ed.*, 2012, **51**, 11496.
236 J. Zhang and L. Dai, *Angew. Chem., Int. Ed.*, 2016, **55**, 13296.
237 X. Wang, J. Wang, D. Wang, S. Dou, Z. Ma, J. Wu, L. Tao, A. Shen, C. Ouyang, Q. Liu and S. Wang, *Chem. Commun.*, 2014, **50**, 4839.
238 Y. Jiao, Y. Zheng, M. Jaroniec and S. Z. Qiao, *J. Am. Chem. Soc.*, 2014, **136**, 4394.
239 J. Wu, M. Liu, P. P. Sharma, R. M. Yadav, L. Ma, Y. Yang, X. Zou, X. D. Zhou, R. Vajtai, B. I. Yakobson, J. Lou and P. M. Ajayan, *Nano Lett.*, 2016, **16**, 466.
240 Y. Jiao, Y. Zheng, K. Davey and S.-Z. Qiao, *Nat. Energy*, 2016, **1**, 16130.
241 N. Chen, X. Huang and L. Qu, *Phys. Chem. Chem. Phys.*, 2015, **17**, 32077.
242 Y. Zheng, Y. Jiao, Y. Zhu, L. H. Li, Y. Han, Y. Chen, A. Du, M. Jaroniec and S. Z. Qiao, *Nat. Commun.*, 2014, **5**, 3783.
243 F. Li, M. Xue, G. P. Knowles, L. Chen, D. R. MacFarlane and J. Zhang, *Electrochim. Acta*, 2017, **245**, 561.
244 H. Wang, Y. Chen, X. Hou, C. Ma and T. Tan, *Green Chem.*, 2016, **18**, 3250.
245 Y. Liu, J. Zhao and Q. Cai, *Phys. Chem. Chem. Phys.*, 2016, **18**, 5491.
246 N. Sreekanth, M. A. Nazrulla, T. V. Vineesh, K. Sailaja and K. L. Phani, *Chem. Commun.*, 2015, **51**, 16061.
247 B. Kumar, M. Llorente, J. Froehlich, T. Dang, A. Sathrum and C. P. Kubiak, *Annu. Rev. Phys. Chem.*, 2012, **63**, 541.
248 M. S. Wrighton, *Science*, 1986, **231**, 32.
249 R. M. Bullock, A. K. Das and A. M. Appel, *Chem. – Eur. J.*, 2017, **23**, 7626.
250 C. Costentin, M. Robert and J.-M. Savéant, *Curr. Opin. Electrochem.*, 2017, **2**, 26.
251 N. Kumagai and M. Shibasaki, *Isr. J. Chem.*, 2017, **57**, 270.
252 S. Meshitsuka, M. Ichikawa and K. Tamaru, *J. Chem. Soc., Chem. Commun.*, 1974, 158.
253 J. Shen, R. Kortlever, R. Kas, Y. Y. Birdja, O. Diaz-Morales, Y. Kwon, I. Ledezma-Yanez, K. J. Schouten, G. Mul and M. T. Koper, *Nat. Commun.*, 2015, **6**, 8177.
254 Z. Weng, J. Jiang, Y. Wu, Z. Wu, X. Guo, K. L. Materna, W. Liu, V. S. Batista, G. W. Brudvig and H. Wang, *J. Am. Chem. Soc.*, 2016, **138**, 8076.
255 X. Zhang, Z. Wu, X. Zhang, L. Li, Y. Li, H. Xu, X. Li, X. Yu, Z. Zhang, Y. Liang and H. Wang, *Nat. Commun.*, 2017, **8**, 14675.
256 X. M. Hu, M. H. Ronne, S. U. Pedersen, T. Skrydstrup and K. Daasbjerg, *Angew. Chem., Int. Ed.*, 2017, **56**, 6468.
257 A. Goeppert, M. Czaun, J. P. Jones, G. K. Surya Prakash and G. A. Olah, *Chem. Soc. Rev.*, 2014, **43**, 7995.
258 J. Albo, M. Alvarez-Guerra, P. Castaño and A. Irabien, *Green Chem.*, 2015, **17**, 2304.
259 I. Ganesh, *Renewable Sustainable Energy Rev.*, 2014, **31**, 221.
260 S. Back, H. Kim and Y. Jung, *ACS Catal.*, 2015, **5**, 965.
261 D. Ren, B. S.-H. Ang and B. S. Yeo, *ACS Catal.*, 2016, **6**, 8239.
262 Y. Wang, M. Hatakeyama, K. Ogata, M. Wakabayashi, F. Jin and S. Nakamura, *Phys. Chem. Chem. Phys.*, 2015, **17**, 23521.

